2020-09-30

Numerical study of implosion of shell structures

Kwon, Y.W.; Sugimoto, S.

Springer

Kwon, Y. W., and S. Sugimoto. "Numerical study of implosion of shell structures." Multiscale and Multidisciplinary Modeling, Experiments and Design 3.4 (2020): 313-336. https://hdl.handle.net/10945/67889

Multiscale and Multidisciplinary Modeling, Experiments and Design (2020) 3:313–336
https://doi.org/10.1007/s41939-020-00078-y

ORIGINAL PAPER

Numerical study of implosion of shell structures

Y. W. Kwon[1] · S. Sugimoto[2]

Received: 25 July 2020 / Accepted: 17 August 2020 / Published online: 30 September 2020

Abstract
To better understand the implosion and the resultant shock wave, a series of numerical modeling and simulations were undertaken for the buckling and collapse of spherical and cylindrical shell structures. The shells were assumed to be made of steel, aluminum, and laminated fibrous composites, respectively. First, the buckling was examined for the shell structures subjected to external pressure loading without any contact with fluid media. Both static and dynamic buckling was studied. For the dynamic buckling, the speed of collapse was controlled to investigate its effect on the buckling characteristics such as buckling mode. This was achieved by decreasing the internal pressure at different rates as the structures were subjected to a constant external pressure. Then, the full implosion process associated with the collapse of shell structures was modelled and studied to understand the shock wave propagation radiated from the collapsing shell structures. The structures were initially subjected to an external water pressure equivalent to a specified water depth. Then, the collapse speed of the shells was controlled, too. Finally, the effect of an initial defect on the buckling and implosion of cylindrical shells was examined. The numerical study compared the implosion characteristics resulting from spherical and cylindrical shells, different material properties, and various controlled collapse speeds. The results suggested that there were optimal parameters which generate the maximum peak pressure during the implosion process.

Keywords Implosion · Buckling · Shock wave · Metals and composites · Initial defect

1 Introduction

When a structure buckles suddenly under a high external water pressure, the collapsing structure produces shock waves propagating back into the surrounding water. The resultant shock wave can be detrimental to any neighboring structure. As a result, research has been conducted to understand and predict the implosion process.

A sudden collapse of a cavity (or bubble) also produces high shock wave back into the surrounding water medium. Therefore, much research has been also conducted for the collapsing bubbles. When a structure has very negligible strength and stiffness, its collapse can be approximated as the collapse of a bubble of the equivalent geometric shape. Thus, the bubble collapse can be considered as an extreme case of implosion.

One of the early studies on the bubble dynamics was conducted by Rayleigh (1917). He developed an analytical solution of a spherical bubble collapsing under an external pressure. The spherical bubble was assumed to have a constant or isothermally changing internal pressure. However, compressible air pressure inside the bubble was not properly considered. Plesset (1949) and Gilmore (1952) further developed the mathematical models for the spherical cavity including compressible air inside the cavity. When the dynamic motion of the cavity boundary was compared, the analytical equations by Plesset and Gilomre agreed well with the numerical solution as the compressible air was modelled inside the cavity (Sugimoto and Kwon 2020). More recently, Kedrinskii (2005) generalized the Gilmore type equation for bubbles of cylindrical or spherical shapes with a compressible liquid. A recent study (Ilinskii 2012) examined the cylindrical bubble pulsation.

✉ Y. W. Kwon
ywkwon@nps.edu

✉ S. Sugimoto
sugimoto.shinichi.xh@cs.atla.mod.go.jp

[1] Department of Mechanical and Aerospace Engineering, Naval Postgraduate School, Monterey, CA 93943, USA

[2] Naval Platform and Signature Research Division, Structure and Material Research Section, Naval Systems Research Center, Acquisition, Technology and Logistics Agency, Tokyo, 1530061, Japan

Early studies of structural implosion were conducted in 1950's and 1960's (Isaacs and Maxwell 1952; Urick 1963). Both studies used the implosion as a source for underwater acoustic signals. Another implosion study (Orr and Schoenberg 1976) was also conducted for the acoustic signal. Later, a series of studies were conducted to examine the shock pressure wave resulting from implosion. Turner and his colleague (Turner 2007; Turner and Ambrico 2012) conducted experimental studies on implosion of a spherical glass and an aluminum cylindrical tube. They measured the shock pressure time-history during the implosion process. A numerical study was conducted for implosion of a cylindrical shell, which was pressurized just below the buckling pressure of the cylinder and a nearby underwater explosion was simulated to initiate the collapse of the cylinder (Krueger 2006). Another numerical study was conducted to validate the numerical model to experimental results (Farhat et al. 2013). More recently, Shukla and his group (Gupta et al. 2014; Pinto et al. 2015, 2018) conducted experiments of composite cylinders as conducted by the numerical study by Krueger (2006). They measured the deformation of collapsing composite cylinders using the digital image correlation technique and measured the shock pressure using the pressure gage, too.

The previous studies provided understanding of the implosion process and its characteristics. The objective of this study was to investigate what parameter and/or condition produced the greatest shock pressure and energy under the same external water pressure. To this end, a series of numerical modeling and simulations were conducted. Three different material such as steel, aluminum, and a laminated composite were studied. Both spherical and cylindrical shells were examined. The buckling/collapse speeds of the shell structures were also varied to determine its effect on the shock pressure wave.

The next section described the computer modeling, and the subsequent two sections presented the numerical results of the spherical and cylindrical shells, respectively. Then, conclusions were followed.

2 Numerical modeling

Implosion of both spherical and cylindrical shells were analyzed numerically using LS-DYNA (LST 2019). Before the implosion study, buckling of the dry shells were investigated without Fluid–Structure Interaction (FSI) to understand the buckling pressure and the buckling characteristics such as buckling modes. After that, the implosion studies were undertaken with FSI.

The nominal internal radius of all shell models was 1 m, and the cylindrical shells had rigid plates at both ends. The materials considered in this study were steel, aluminum, and a carbon fiber composite, respectively. Both steel and aluminum were assumed to be elastic and perfectly plastic, whose material properties are listed in Table 1. As a result, the straining hardening was neglected for both materials for conservative modelling and simplicity. The composite cylinders were modelled as a laminated composite. The material property of the lamina is shown in Table 2. The Chang-Chang failure criteria were used for the failure of the composite material, and their failure strengths were also given in Table 2.

Table 1 Material properties of steel and aluminum

Material	Steel	Aluminum
Young's modulus, E	206 GPa	68.9 GPa
Poisson' ratio, υ	0.3	0.3
Critical buckling pressure, P_{cr}	0.997 MPa	0.334 MPa
Critical stress, σ_{cr}	249 MPa	83.4 MPa
Yield stress, σ_Y	350 MPa	276 MPa

Table 2 Material properties of fibrous composite lamina

Material	CFRP
Density	1304 kg/m^3
Young's modulus of the longitudinal fibers, E1	139 GPa
Young's modulus of the transverse fibers, E2	7.2 GPa
Shear modulus, G12	3.5 GPa
Shear modulus, G23	2.4 GPa
Major poisson's ration, ν_{12}	0.235
Poisson's ration, ν_{23}	0.500
Ultimate tensile strength 0°, XT	1500 MPa
Ultimate comp. strength 0°, XC	1200 MPa
Ultimate tensile strength 90°, YT	50 MPa
Ultimate comp. strength 90°, YC	250 MPa
Ultimate in-plane shear strength., SC	70 MPa

The four-node shell elements called thin shell elements were used for all analyses, which have three displacements and three rotations at every node. The solid-like shell elements called thick shell elements were also considered, which has the nodal degrees of freedom like a 3-D solid element. This type of element is easier for coupling with the fluid elements on the inner and outer surfaces of the shell element. The solid-like shell elements gave very close solutions to the standard shell elements, but it took much longer computational times for the former elements. Therefore, the standard shell elements were used throughout the study unless mentioned otherwise.

Structured Arbitrary Lagrange Euler (S-ALE) solver in LS-DYNA was used in the water and air regions for all FSI analyses. The S-ALE solver is recently added into LS-DYNA and has several advantages over the generic ALE solver. It runs faster and uses less memory and more stable. Bi-

directional FSI coupling of water and air was used for all FSI problems.

As a parametric study, the speed of the buckling/collapse was controlled. This was conducted by applying internal pressure to the shell and decreasing the internal pressure at different rates. Another simulation was the change of the mass density of the material. This was an arbitrary increase of the density up to five times from its nominal values. The main purpose of these studies was to determine how the buckling/collapse speed influenced the buckling characteristics and the resultant shock wave propagation during the implosion process. For example, strain hardening of the materials as well as other possible internal structures could delay the buckling/ collapse speed. Thus, the parametric study was to simulate those situations.

For the dry shell structures, both external and internal pressures were applied using the external loading option. However, for the structures with FSI, pressure loading was applied through the fluid media in contact with the structure. The external fluid was water, while the internal fluid was air. The water pressure was assumed such that the shell structure was placed in a certain water depth with the proper hydrostatic pressure. The air pressure was assumed at the atmospheric pressure condition.

The Gruneisen equation of state was used to model the water medium. The equation of state is expressed as below:

$$p = \frac{\rho_o C^2 \mu\left[1 + \left(1 - \frac{\gamma_o}{2}\right)\mu - \frac{a}{2}\mu^2\right]}{\left[1 - (S_1 - 1)\mu - S_2\frac{\mu^2}{\mu+1} - S_3\frac{\mu^3}{(\mu+1)^2}\right]} + \left[\gamma_o + a\mu\right]E. \tag{1}$$

In this study, the following material constants were used. Water was assumed to have the mass density $\rho_o = 1000\,\text{kg/m}^3$ and the speed of sound $C = 1490$ m/s. Other constants for the equation of state were assumed $S_1 = 1.79$, $S_2 = S_3 = 0$, $\gamma_0 = 1.65$, $a = 0$. Furthermore, the ratio of density change was expressed as $\mu = \frac{\rho}{\rho_o} - 1$ with the present density ρ, and E is the internal energy which is dependent on the water depth.

The polynomial equation of state was used to model the air inside the shell structure, and it is given as below:

$$p = C_0 + C_1\mu + C_2\mu^2 + C_3\mu^3 + \left(C_4\mu^4 + C_5\mu^5 + C_6\mu^6\right)E. \tag{2}$$

The material constants for this equation of state were assumed such that $C_0 = C_1 = C_2 = C_3 = C_6 = 0.0$, and $C_4 = C_5 = 0.403$. In addition, the density of air was assumed $1.293\,\text{kg/m}^3$, E is the internal energy and $\mu = \frac{1}{V} - 1$ where V is the relative volume.

3 Spherical shell

This section studied the implosion characteristics resulting from the collapse of spherical shells. Collapse of shell structures can be initiated from different failure modes, which could be elastic buckling or plastic deformation depending on which failure mode occurs at the lower load level.

The spherical shell was made of either steel or aluminum materials whose properties were provided in Table 1. Both materials were assumed to be perfect plastic without strain hardening. The surrounding water was modeled using the Gruneisen equation as stated previously. Inside of the shell was assumed to have atmospheric pressure.

First, the critical bucking pressure p_{cr} of a dry thin-walled spherical shell was computed using the following equation (Timoshenko and Gere 1961):

$$p_{cr} = \frac{2E}{\sqrt{3(1-\nu^2)}}\left(\frac{t}{R}\right)^2, \tag{3}$$

where E and ν are elastic modulus and Poisson's ratio, and R and t are the shell inner radius and thickness, respectively. The elastic critical stress σ_{cr} for a thin spherical shell is computed from

$$\sigma_{cr} = \frac{p_{cr}R}{2t}. \tag{4}$$

Based on the von Mises yield criterion, the spherical shell does not yield if the critical stress σ_{cr} is less than the yield strength of the material. In that case, elastic buckling is the initiation of the collapse followed by plastic deformation.

The shell thickness was 2 mm. In this case, the critical buckling stress was less than the yield strength of each material. Therefore, the shell will collapse through elastic buckling rather than plastic deformation. To confirm the critical buckling load, finite element analyses were also conducted using the mesh of a half spherical shell with symmetric boundaries as sketched in Fig. 1. The numerical buckling pressure agreed very well with the analytical solutions for

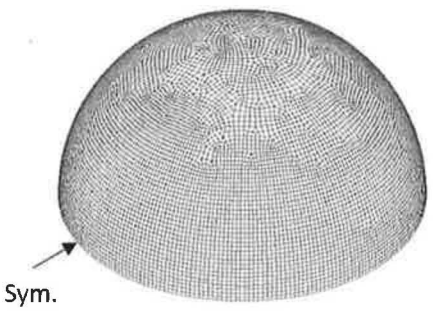

Fig. 1 A half model of spherical shell with symmetric plane

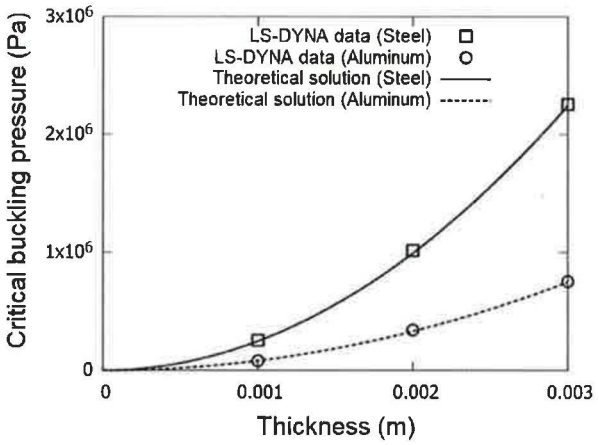

Fig. 2 Buckling pressure of spherical shells

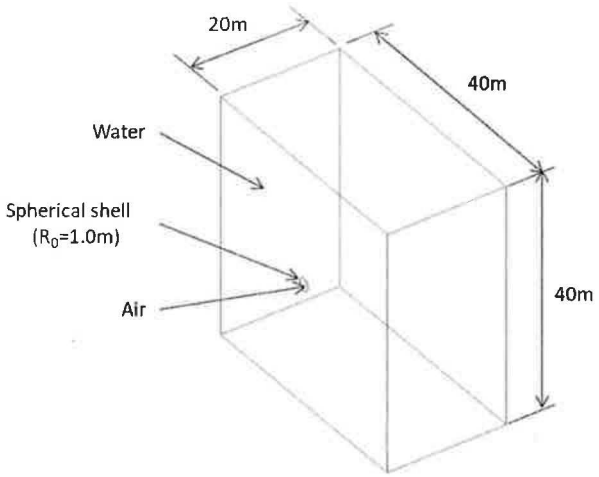

Fig. 3 Overall sketch for implosion study of spherical shell

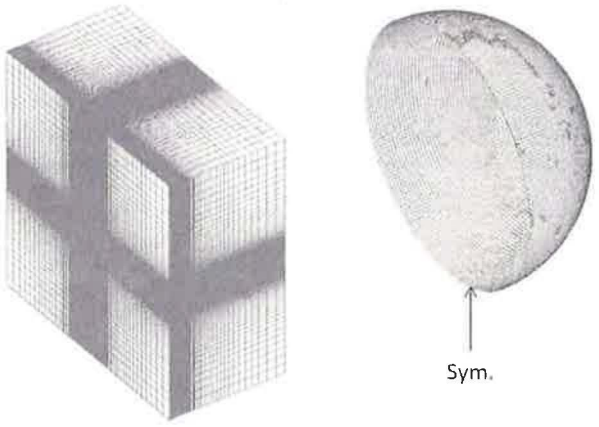

Fig. 4 Finite element meshes of water domain and spherical shell

both aluminum and the steel spherical shells for various thicknesses as shown in Fig. 2 (Timoshenko and Gere 1961).

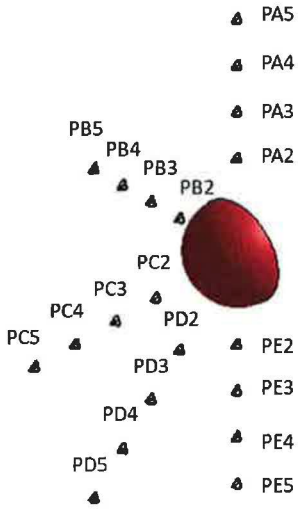

Fig. 5 Numerical probe locations around the spherical shell

Figure 3 shows the sketch of the implosion study of the spherical shell. The finite element meshes of the fluid (water) domain and the spherical shell are shown in Fig. 4 The location of the numerical pressure probe for the spherical shell model is shown in Fig. 5, and the detailed locations of all the probes are listed in Tables 3 and 4. In addition, Table 5 shows the geometric properties of both steel and aluminum spherical shells of 2 mm thick as well as the buckling pressure, critical buckling stress, and both external and internal pressure of the spherical shells. Internal pressure was applied to the spherical shells as an external loading so that the buckling and collapse could be controlled as explained in the last section. The internal pressure was decreased as a function of time, and the reduction rate of the internal pressure was controlled to determine its effect of the implosion characteristics.

The external pressure was decided as one and a half times of the critical buckling pressure of spherical shell made of steel. The rate of reduction of the internal pressure was varied by deciding the final time to reach the zero applied internal pressure as sketched in Fig. 6. The applied internal pressure became zero at $Dt = 0.1$ ms, 5 ms, 10 ms, and 15 ms, respectively.

As the spherical shell collapsed significantly, the deformed shape became so complicated with buckling, plastic deformation, and potential self-contacts of the collapsed surface. As a result, when the collapsing process continued before reaching the final collapsed geometry, the analysis program was terminated with an error message stating too much distortions of some finite elements. Unfortunately, remeshing was not possible for this situation. Therefore, one option was to use the element erosion option, i.e., an element was removed when the strain of the element exceeded any

Table 3 Locations of numerical probes outside the spherical shell

No.	Probe	Radial distance (m)	X (m)	Y (m)	Z (m)
1	PA2	2.00	0.00	0.00	2.00
2	PB2	2.00	1.41	0.00	1.41
3	PC2	2.00	2.00	0.00	0.00
4	PD2	2.00	1.41	0.00	− 1.41
5	PE2	2.00	0.00	0.00	− 2.00
6	PF2	2.00	1.00	1.00	1.41
7	PG2	2.00	1.41	1.41	0.00
8	PH2	2.00	1.00	1.00	− 1.41
9	PI2	2.00	1.00	− 1.00	1.41
10	PJ2	2.00	1.41	− 1.41	0.00
11	PK2	2.00	1.00	− 1.00	− 1.41
12	PA3	3.00	0.00	0.00	3.00
13	PB3	3.00	2.12	0.00	2.12
14	PC3	3.00	3.00	0.00	0.00
15	PD3	3.00	2.12	0.00	− 2.12
16	PE3	3.00	0.00	0.00	− 3.00
17	PF3	3.00	1.50	1.50	2.12
18	PG3	3.00	2.12	2.12	0.00
19	PH3	3.00	1.50	1.50	− 2.12
20	PI3	3.00	1.50	− 1.50	2.12
21	PJ3	3.00	2.12	− 2.12	0.00
22	PK3	3.00	1.50	− 1.50	− 2.12
23	PA4	4.00	0.00	0.00	4.00
24	PB4	4.00	2.83	0.00	2.83
25	PC4	4.00	4.00	0.00	0.00
26	PD4	4.00	2.83	0.00	− 2.83
27	PE4	4.00	0.00	0.00	− 4.00
28	PF4	4.00	2.00	2.00	2.83
29	PG4	4.00	2.83	2.83	0.00
30	PH4	4.00	2.00	2.00	− 2.83
31	PI4	4.00	2.00	− 2.00	2.83
32	PJ4	4.00	2.83	− 2.83	0.00
33	PK4	4.00	2.00	− 2.00	− 2.83
34	PA5	5.00	0.00	0.00	5.00
35	PB5	5.00	3.54	0.00	3.54
36	PC5	5.00	5.00	0.00	0.00
37	PD5	5.00	3.54	0.00	− 3.54
38	PE5	5.00	0.00	0.00	− 5.00
39	PF5	5.00	2.50	2.50	3.54
40	PG5	5.00	3.54	3.54	0.00
41	PH5	5.00	2.50	2.50	− 3.54
42	PI5	5.00	2.50	− 2.50	3.54
43	PJ5	5.00	3.54	− 3.54	0.00
44	PK5	5.00	2.50	− 2.50	− 3.54

Table 4 Locations of numerical probe in and near the spherical shell

No.	Probe	Radial distance (m)	X (m)	Y (m)	Z (m)
45	P1	0.01	0.01	0.00	0.01
46	P11	0.14	0.10	0.00	0.10
47	P12	0.21	0.15	0.00	0.15
48	P13	0.28	0.20	0.00	0.20
49	P14	0.42	0.30	0.00	0.30
50	P15	0.57	0.40	0.00	0.40
51	P16	0.71	0.50	0.00	0.50
52	P17	0.85	0.60	0.00	0.60
53	P18	0.99	0.70	0.00	0.70
54	P19	1.13	0.80	0.00	0.80
55	P20	1.27	0.90	0.00	0.90
56	P21	1.41	1.00	0.00	1.00

Table 5 Material and geometric properties of metallic spherical shells

Material	Steel	Aluminum
Radius, R_0	1.0 m	1.0 m
Thickness, t	2 mm	2 mm
Critical buckling pressure, P_{cr}	0.997 MPa	0.334 MPa
Critical stress, σ_{cr}	249 MPa	83.4 MPa
Yield stress, σ_Y	350 MPa	276 MPa
Pressure at yield of material, P_Y	1.4 MPa	1.1 MPa
Buckling mode	Elastic buckling ($P_{cr} < P_Y$)	Elastic buckling ($P_{cr} < P_Y$)
External pressure, P_0	1.5 MPa	1.5 MPa
Initial internal pressure, P_{in} (Load)	1.4 MPa	1.4 MPa

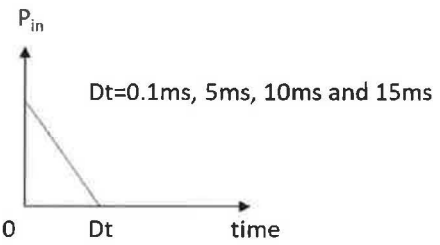

Fig. 6 Pressure time history at different locations of the spherical cavity

specified value, typically the failure strain. When the element erosion option was used, the analysis continued beyond the complete collapse of the shell structures.

Figure 7 shows the normalized pressure for the spherical steel shell with the initial inner radius 1 m and the wall thickness 2 mm. The applied internal pressure was reduced

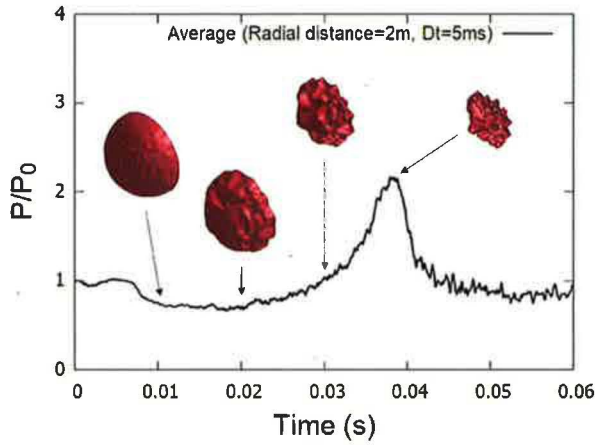

Fig. 7 Normalized pressure time-history of a spherical steel shell with inner radius 1 m, thickness 2 mm and Dt = 5msec at 2 m of radial distance

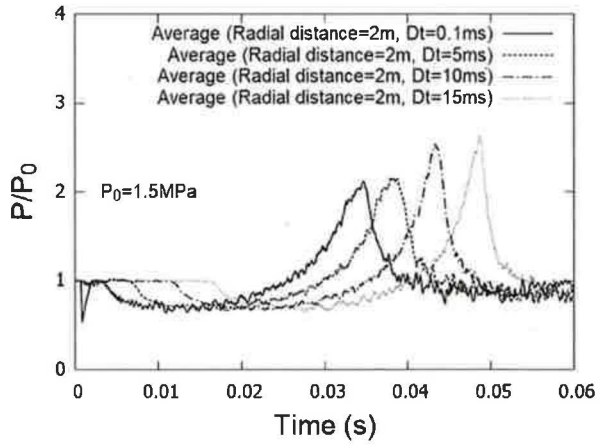

Fig. 8 Comparison of the normalized pressure time-histoies for four different reduction rates of internal pressure as shown in Fig. 6 for spherical steel shell with inner radius 1 m, thickness 2 mm at 2 m of radial distance

linearly to zero with $Dt = 5$ ms. The pressure was normalized with respect to the initial external pressure in the surrounding water and the pressure shows an average of pressure probes which are located at the same radial distance. The pressure remained relatively the same until around 7 ms and the pressure decreased for a while, which was followed by almost a constant pressure as the shell collapsed with moderate amounts until around 23 ms. As the collapse continued further, the pressure increased in the exponential curve with the maximum pressure just before 40 ms. The peak pressure was approximately 2.2 times the initial water pressure. Before reaching the peak pressure, some elements were deleted with the erosion option. The collapsed shell at the peak of the pressure shows some deleted elements in Fig. 7. Once the peak

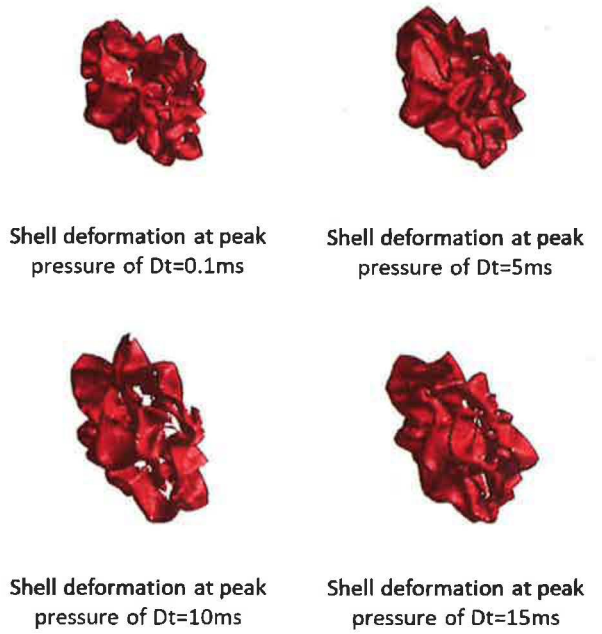

Fig. 9 Comparison of collapsed shapes of the spherical steel shell with inner radius 1 m and thickness 2 mm for three different reduction rates when the pressure at gage PA2 reached the maximum

pressure reached, the pressure also decreased in the negative exponential curve shape.

Figure 8 compares the pressure time-histories for four different reduction rates of the internal pressure applied to the same steel shell as discussed above. Figure 9 shows the collapsed shapes of the spherical steel shell with inner radius 1 m and thickness 2 mm for three different reduction rates when the pressure reached the maximum value. The pressure plots in Fig. 8 clearly show the delay of the buckling as the reduction rate of the applied internal pressure becomes slower, as expected. The peak pressure also occurred later with the slower reduction rate of the internal pressure. However, the peak pressure was higher as the reduction rate of the internal pressure became slower. This was unexpected initially. The faster collapse of the spherical shell structure was expected to result in greater pressure. However, as shown later, other shells also showed that there was an optimal buckling speed to result in the greatest shock pressure radiated from the collapsing shell.

A spherical aluminum shell was studied next. The normalized pressure time-history was plotted in Fig. 10 for the spherical aluminum shell with inner radius 1 m and thickness 2 mm. The general trend of the pressure time-history was similar between the spherical aluminum and steel shells.

Figure 11 shows comparison of normalized pressure time-history between spherical steel shell and spherical aluminum shell with 5 ms of reduction rates. As expected, the peak pressure of spherical aluminum shell was higher than one of

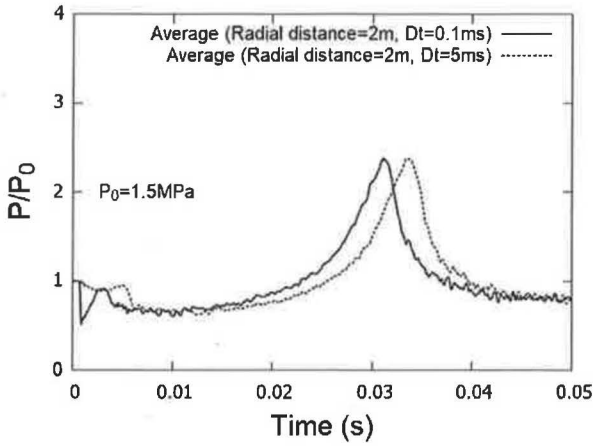

Fig. 10 Normalized pressure time-history of spherical aluminum shell with inner radius 1 m and thickness 2 mm for different reduction rates of applied internal pressure at 2 m of radial distance

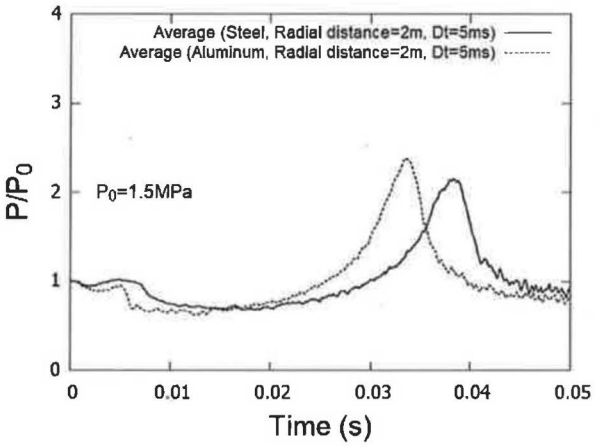

Fig. 11 Comparison of Normalized pressure time-history between spherical steel shell and spherical aluminum shell with 5 ms of reduction rates

spherical steel shell and occurred earlier. This result shows that strength and stiffness of shell affect pressure character resulted from implosion.

4 Cylindrical shells

4.1 Buckling study

The nominal cylindrical shell was 4 m long with the inner radius 1 m and thickness 20 mm. Table 6 lists all the geometric properties and various pressures of the nominal steel and aluminum cylindrical shells. Table 2 shows the material properties of the composite lamina which was used for the composite cylinder with the layup orientations [(±85°), (±45°), (±15°)]. All the cylindrical shells were assumed

Table 6 Material and geometric properties of metallic cylindrical shells

Material	Steel	Aluminum
Radius, R_0	1.0 m	1.0 m
Length, L	4.0 m	4.0 m
Thickness, t	20 mm	20 mm
Yield stress, σ_Y	350 MPa	276 MPa
Critical buckling pressure, P_{cr}	4.08 MPa	1.36 MPa
Circumferential wave number, n	4	4
Pressure at yield of material, P_Y	7.0 MPa	5.52 MPa
External pressure, P_0	6.1 MPa	6.1 MPa
Initial internal pressure, P_{in}	6.0 MPa	6.0 MPa

to have rigid end plates such that only the side wall would buckle and collapse. Because there was no theoretical solution to the buckling pressure of the cylindrical shell with rigid end plates, the finite element analysis was conducted to determine the critical pressure for buckling.

The analytical solution for a cylindrical metallic shell with simply supported edges was given as below (Windenburg and Trilling 1934):

$$p_{cr} = \frac{Et\alpha^4}{R\left(n^2+0.5\alpha^2-1\right)\left(n^2+\alpha^2\right)^2} + \frac{E}{12\left(1-\nu^2\right)}\left(\frac{t}{R}\right)^3\frac{\left(n^2+\alpha^2-1\right)^2}{n^2+0.5\alpha^2-1}, \tag{5}$$

where E is the elastic modulus, R is the radius, t is the thickness, ν is Poisson's ratio, n is the circumferential wave number, and α is the nondimensional parameter related to the ratio of the radius R to the length L of the cylinder as defined below:

$$\alpha = \frac{\pi R}{L}. \tag{6}$$

Figure 12 shows the critical buckling pressure of the simply supported steel and aluminum cylinders with the nominal dimensions for different circumferential wave numbers. Those buckling pressures were computed using Eq. (5). The results indicated that the lowest critical buckling pressure occurred with n equal to 4. Therefore, the buckling pressure of the cylindrical shells with simply supported edges was compared to the same cylinders with rigid end plates, which represents clamped edged. Table 7 shows the comparison of the critical buckling pressures of the steel and aluminum cylinders with simply supported and clamped edges. The solutions for the former boundary condition was computed using Eq. (5), while the solutions for the latter boundary condition were computed using the finite element analysis. The steel cylinder had an increase in the critical buckling pressure by around 50% as the boundary condition changed from

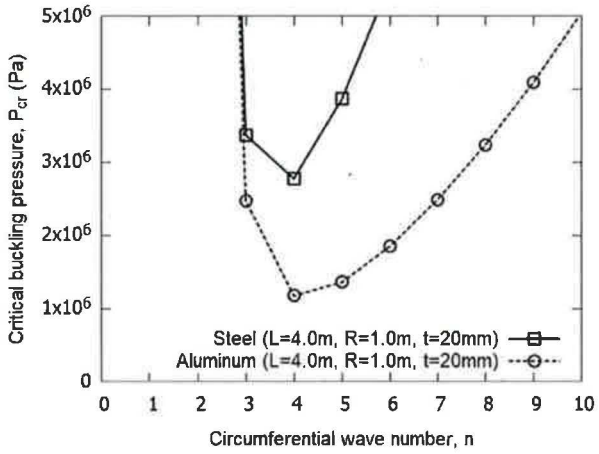

Fig. 12 Buckling pressure of steel and aluminum cylinders with simply supported edges

Table 7 Comparisons of critical buckling pressure for two different boundary conditions

	Steel		Aluminum	
	LS-DYNA (cylinder with rigid lids)	Theoretical solution (simply supported cylinder)	LS-DYNA (cylinder with rigid lids)	Theoretical solution (simply supported cylinder)
P_{cr}	4.08 MPa	2.77 MPa	1.36 MPa	1.17 MPa
n	4	4	4	4

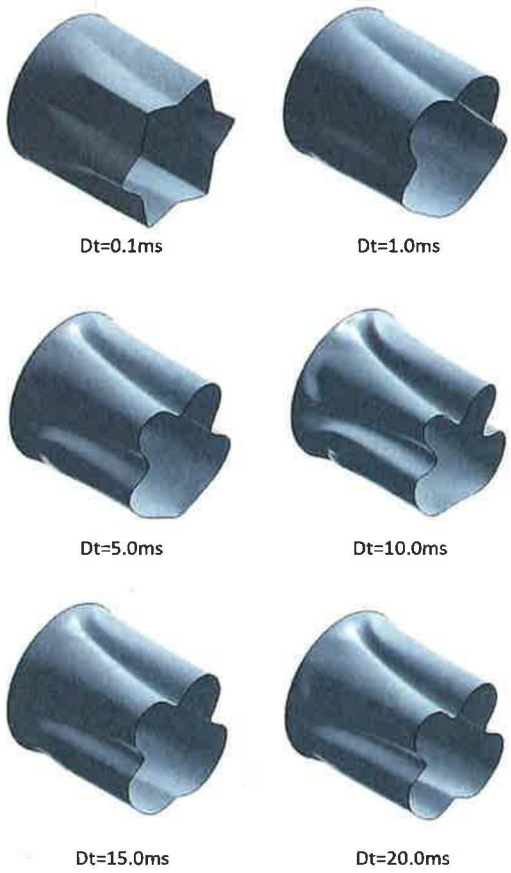

Fig. 13 Buckling shapes of steel cylinder as the internal pressure decreased in different rates without FSI

the simply supported to clamped edges. On the other hand, the aluminum cylinder showed about 15% increase with the change of the edge condition. Furthermore, the ratio of the critical buckling pressure of the steel cylinder to the aluminum cylinder was greater for the clamped edges than for the simply supported edges. The former had the ratio of 3 and the latter had the ratio of 2.4. The elastic modulus of the steel is about 3 times greater than that of the aluminum. Therefore, the ratio of the buckling pressure of the clamped steel and aluminum cylinders was the same as the ratio of elastic modulus.

The buckling pressure of the composite cylinder of the same geometric dimensions with clamped ends was computed using the finite element analysis. The critical buckling pressure was 0.63 MPa. This value was much lower than those of the steel and aluminum cylinders.

The previous buckling study was for the static buckling. To investigate the dynamic buckling of the cylindrical shells, they were subjected to both external and internal pressure initially using the external loading option. The external pressure remained the same, while the internal pressure was reduced in terms of time as sketched in Fig. 6. As the reduction rate of the internal pressure was varied, the buckling mode also changed. Figure 13 shows the cross sections at the mid-length of the steel cylinder as the reduction rate of internal pressure was varied. When the internal pressure was reduced very quickly ($Dt = 0.1$ ms), the buckling mode was $n = 6$, i.e., wave number of six. When $Dt = 1.0$ ms or 5.0 ms, the mode shape was changed to $n = 5$. As the reduction rate was further decreased, the mode shape became $n = 4$. In other words, the buckled mode shape became the same as the static bucked mode shape as the internal pressure reduced slowly.

Because the reduction rate of the internal pressure controls the speed of the buckling, the mass of the cylinder was varied to determine whether the change in mass had similar effect like the change in the internal pressure. As a result, the mass density of the steel cylinder was varied arbitrarily up to five times of its original density. The change in the density slowed the buckling but did not change the mode shapes as shown in Fig. 14. All the cases showed the buckling mode of $n = 6$. Thus, the change in the mass density did not produce the same effect as the control of internal pressure.

Figure 15 shows the average velocity in the radial direction as the mass density was varied up to five times of the orig-

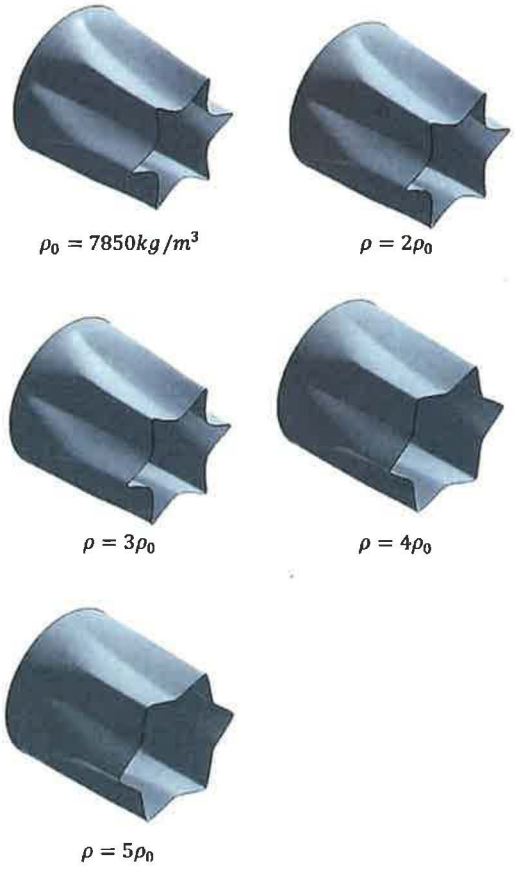

Fig. 14 Buckling shapes of steel cylinder with different assumed densities without FSI

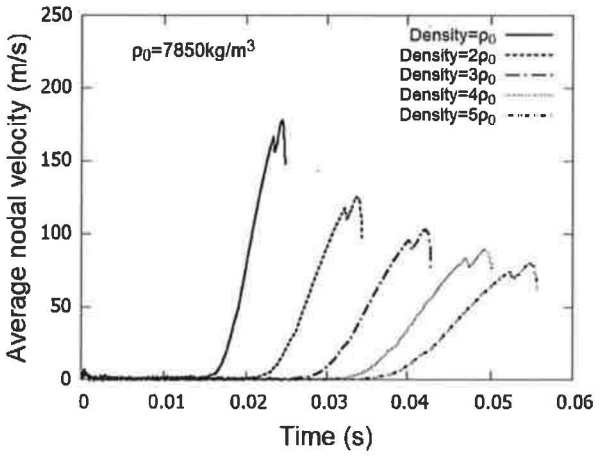

Fig. 15 Average radial velocity of the mid-section of the steel cylinder with arbitrarily assumed mass densities

inal density. The average velocity was computed using the nodal velocities along the circumference at the mid-section of the cylinder. When the cylinder had the original mass, the velocity was very small until around 15 ms, and the velocity

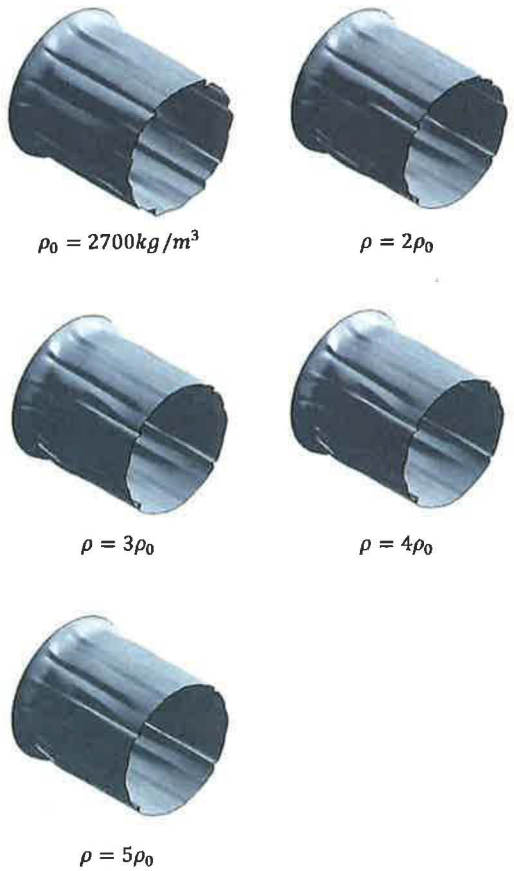

Fig. 16 Cross-sectional shapes of aluminum cylinders with different mass densities without FSI

increased very rapidly until it reached the maximum value which was followed steep drop. Before reaching the maximum average velocity, there was a very small temporary decrease. The maximum velocity occurred at around 22 ms. As the mass density increased, the steep increase of the velocity was further delayed with a lower maximum velocity. Thus, the mass density influenced the radial velocity of the shell motion. Even though the increase of the mass density delayed the buckling speed like the controlling the internal pressure, the former did not affect the buckling mode shape, while the latter did.

The aluminum cylinder showed no major change in its buckling shape as its density was arbitrarily varied up to five times of the original value. Figure 16 shows the buckling shapes of five different mass densities of the aluminum cylinder. Figure 17 also shows the buckling shapes of the carbon fiber composite cylinder as the density was arbitrarily varied up to five times. Some change in the buckling shapes was observed with different densities of the composite.

The maximum average radial velocity of the mid-section of every cylinder was plotted in Fig. 18 for the steel, alu-

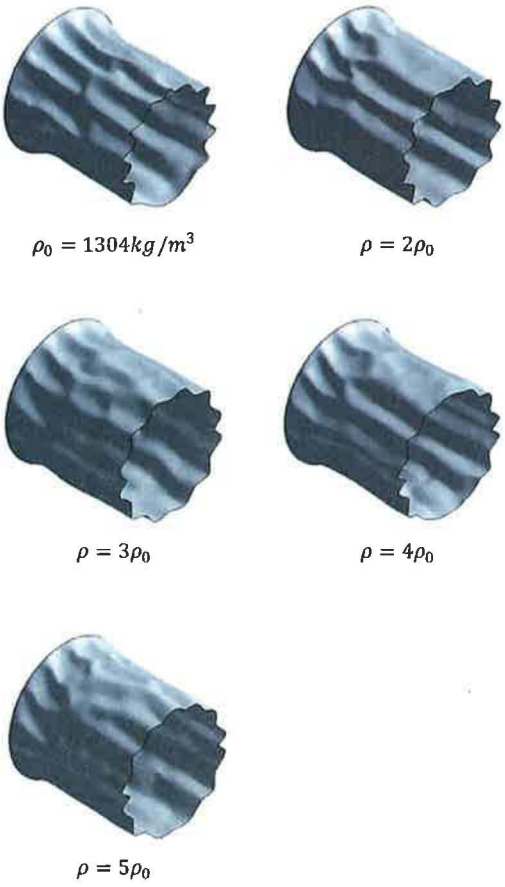

Fig. 17 Cross-sectional shapes of composite cylinders with different mass densities without FSI

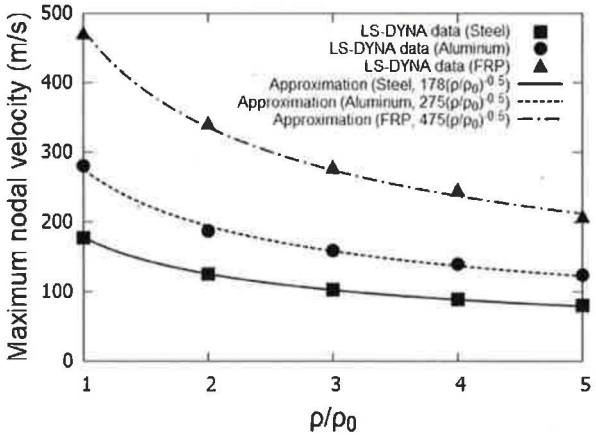

Fig. 18 Plot of maximum average radial velocity at the mid-section of steel, aluminum and composite cylinders as the mass density increased

minum and composite cylinders as their original mass density was arbitrarily increased. Because the composite had the lowest density among the three, its maximum radial velocity was the greatest than the other cylinders. As seen in the figure,

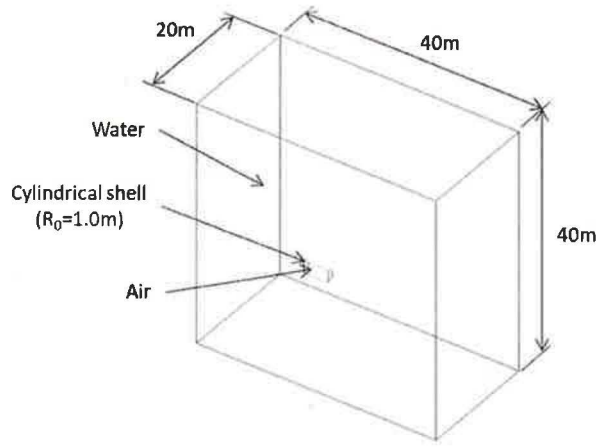

Fig. 19 Sketch of the computer model of a cylindrical shell for implosion study

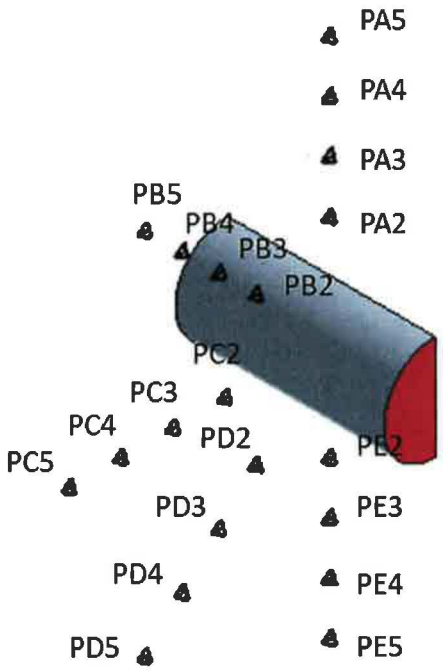

Fig. 20 Gage locations for the implosion model of a cylindrical shell

the decrease in the maximum velocity was inversely proportional to the one-half power of the density ratio $\frac{\rho}{\rho_o}$ where subscript 'o' indicates the original density. As the density increased fourfold, the maximum collapse speed decreased by half.

4.2 Implosion of steel cylinders

Once the buckling characteristics of the cylindrical shells were examined, the next study was undertaken for the implosion of the cylindrical shells. Figure 19 describes the problem

Table 8 Locations of numerical probes outside the cylindrical shell

No.	Probe	Radial distance (m)	*X* (m)	*Y* (m)	*Z* (m)
1	PA2	2.00	0.00	0.00	2.00
2	PB2	2.00	1.41	0.00	1.41
3	PC2	2.00	2.00	0.00	0.00
4	PD2	2.00	1.41	0.00	− 1.41
5	PE2	2.00	0.00	0.00	− 2.00
6	PF2	2.00	0.00	1.00	2.00
7	PG2	2.00	1.41	1.00	1.41
8	PH2	2.00	2.00	1.00	0.00
9	PI2	2.00	1.41	1.00	− 1.41
10	PJ2	2.00	0.00	1.00	− 2.00
11	PK2	2.00	2.00	2.00	0.00
12	PA3	3.00	0.00	0.00	3.00
13	PB3	3.00	2.12	0.00	2.12
14	PC3	3.00	3.00	0.00	0.00
15	PD3	3.00	2.12	0.00	− 2.12
16	PE3	3.00	0.00	0.00	− 3.00
17	PF3	3.00	0.00	1.00	3.00
18	PG3	3.00	2.12	1.00	2.12
19	PH3	3.00	3.00	1.00	0.00
20	PI3	3.00	2.12	1.00	− 2.12
21	PJ3	3.00	0.00	1.00	− 3.00
22	PK3	3.00	3.00	2.00	0.00
23	PA4	4.00	0.00	0.00	4.00
24	PB4	4.00	2.83	0.00	2.83
25	PC4	4.00	4.00	0.00	0.00
26	PD4	4.00	2.83	0.00	− 2.83
27	PE4	4.00	0.00	0.00	− 4.00
28	PF4	4.00	0.00	1.00	4.00
29	PG4	4.00	2.83	1.00	2.83
30	PH4	4.00	4.00	1.00	0.00
31	PI4	4.00	2.83	1.00	− 2.83
32	PJ4	4.00	0.00	1.00	− 4.00
33	PK4	4.00	4.00	2.00	0.00
34	PA5	5.00	0.00	0.00	5.00
35	PB5	5.00	3.54	0.00	3.54
36	PC5	5.00	5.00	0.00	0.00
37	PD5	5.00	3.54	0.00	− 3.54
38	PE5	5.00	0.00	0.00	− 5.00
39	PF5	5.00	0.00	1.00	5.00
40	PG5	5.00	3.54	1.00	3.54
41	PH5	5.00	5.00	1.00	0.00
42	PI5	5.00	3.54	1.00	− 3.54
43	PJ5	5.00	0.00	1.00	− 5.00
44	PK5	5.00	5.00	2.00	0.00

Table 9 Locations of numerical probe in and near the cylindrical shell

No.	Probe	Radial distance (m)	*X* (m)	*Y* (m)	*Z* (m)
45	P1	0.01	0.01	0.00	0.01
46	P11	0.14	0.10	0.00	0.10
47	P12	0.21	0.15	0.00	0.15
48	P13	0.28	0.20	0.00	0.20
49	P14	0.42	0.30	0.00	0.30
50	P15	0.57	0.40	0.00	0.40
51	P16	0.71	0.50	0.00	0.50
52	P17	0.85	0.60	0.00	0.60
53	P18	0.99	0.70	0.00	0.70
54	P19	1.13	0.80	0.00	0.80
55	P20	1.27	0.90	0.00	0.90
56	P21	1.41	1.00	0.00	1.00

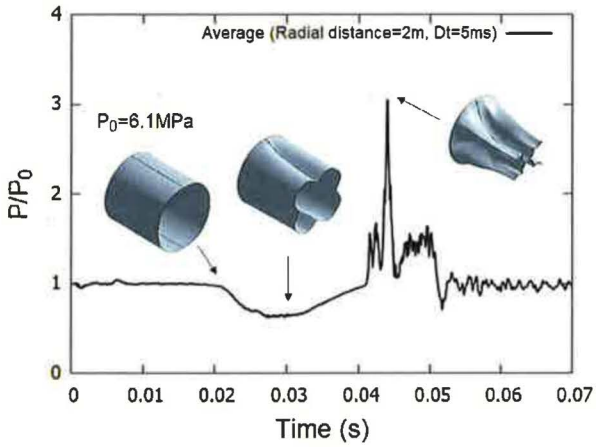

Fig. 21 Normalized pressure time-history of a cylindrical steel shell with inner radius 1 m, thickness 20 mm and $Dt = 5$msec

domain which consists of a cylindrical shell with air inside and water outside of the shell. Non-reflective boundary conditions were applied to the boundary of the water medium. A half of the whole domain was modelled with symmetry for computational efficiency. The cylindrical shell was also modelled as a half cylinder. This suggests that any odd wave number of buckling mode shape cannot be represented with the symmetric model.

Figure 20 illustrates the gage locations, where pressure time-histories were obtained. Tables 8 and 9 provided exact coordinate values of the gage locations which are located inside and outside of the cylinder. The external pressure in the water was set 1.5 times of the critical static buckling pressure of the cylinder. The internal pressure was also applied initially and decreased linearly as sketched in Fig. 6.

Figure 21 shows the pressure time-history of the nominal steel cylinder which is the average pressure of the five gages from #PA2 to #PE2 at the same radial distance. The pressure

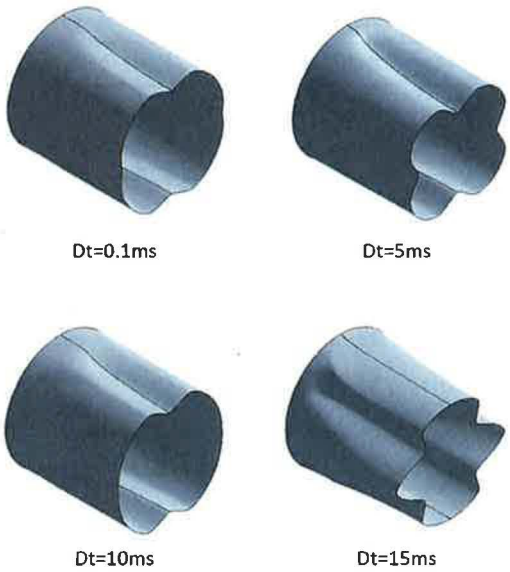

Fig. 22 Buckled mode shapes of steel cylinder under water as the inetrnal pressure decreased in different rates with FSI

was normalized with respect to the initial water pressure, and the internally applied pressure was reduced with $Dt = 5$ ms.

The pressure remained nearly constant until 20 ms. Then, the pressure decreased gradually until 30 ms and increased gradually until around 40 ms. The buckling mode shape at 30 ms shows $n = 4$. After 40 ms, the pressure increased drastically with some oscillation with the maximum pressure at around 43 ms. The maximum pressure was approximately 3.0 times greater than the initial external water pressure. After the maximum pressure, it dropped very quickly. At 50 ms, the pressure returned to the initial pressure with some oscillations. The buckled shape of the steel cylinder was also shown in Fig. 22. The cylindrical shell model did not consider the erosion option to delete elements. Figure 21 also shows the first self-contact of the buckled steel cylinder because of buckling.

The reduction rate of the internal pressure was also varied. Then, the buckling mode shape of the steel cylinder was varied with the change in the reduction rate of the internal pressure as sketched in Fig. 22. Figures 13 and 22 are different in two aspects. Figure 13 used the whole cylinder model, while Fig. 22 was based on a half cylinder. More importantly, the results in Fig. 13 were obtained without FSI. In other words, a constant external pressure was applied to the structure directly and remained all the time. On the contrary, the analysis for Fig. 22 included the FSI such that the external pressure could vary with time as the pressure in the fluid medium. Because of the symmetry model, the odd number of mode shape could not be represented. At any rate of Dt, the buckling with FSI also showed either the mode shape $n = 2$ or $n = 4$ depending on the rate change in the internal pressure. Figure 22 shows the full cylinder with mirror images of the half cylinder. The line in the cylinder indicates the symmetric line of the cylinder.

Figure 23 shows the pressure time-history of the steel cylinder at different radial distance when $Dt = 0.1$ ms, i.e., a very quick reduction, while Fig. 24 shows the same with $Dt = 15$ ms, a much slower reduction of internal pressure. When the pressure was compared for all different Dt rates, an interesting observation was made. As seen in Fig. 25, the reduction rate with $Dt = 5$ ms resulted in the largest peak pressure than any other rate. In other words, the quickest reduction with $Dt = 0.1$ ms did not necessarily produce the larger pressure than that with $Dt = 5$ ms. In addition, the cases with $Dt = 0.1$ ms and 10 ms produced almost the same peak pressures. This observation suggested there was an optimal collapse condition for the cylindrical steel shell to generate the largest pressure during its implosion process. To better understand the result, the radial velocity at the mid-section along the cylinder was plotted in Fig. 26. This was the average radial velocity along the circumference of the lengthwise mid-section of the cylindrical shell. The radial velocity was very small initially for all the cases, but the case with $Dt = 5$ ms showed that the radial velocity increased faster at an earlier time, and decreased faster at an earlier time than other cases. The maximum velocity was close for the cases $Dt = 0.1$, 5, and 10 ms, while that was the largest at $Dt = 15$ ms.

The maximum areal shock energy density rate was examined in Fig. 27. The areal energy density rate was computed from the product of the pressure and fluid velocity. The plot was made at various gage locations around the circumference at the same radial distance as Dt was varied. From the time-history of the areal shock energy density rate, their maximum values were selected for each location for every Dt case and they were plotted in Fig. 27. The plot shows that the maximum areal shock energy density rate was the largest and quite uniform around the circumference with $Dt = 5$ ms, and this was consistent with the peak pressure which was also the largest at $Dt = 5$ ms.

Instead of controlling the internal pressure, the mass density of the steel was arbitrarily varied as before. It was increased to three and five times of the original density, respectively. The change in the density also influences the buckling speed like the control of the internal pressure. Like the change in the internal pressure reduction rate, the change in the mass density also affected the buckled shape of the cross section. Figure 28 shows the buckled cross-sectional shapes of the steel cylinder with three different mass densities. The buckled cross-section was quite dependent on the mass density, i.e., the collapsing speed of the shell. In other words, a change in the collapsing speed of the cylindrical shell with FSI influenced the buckling mode shape. Comparing Figs. 14, 15, 16, 17, 18, 19, 20, 21, 22, 23, 24, 25, 26,

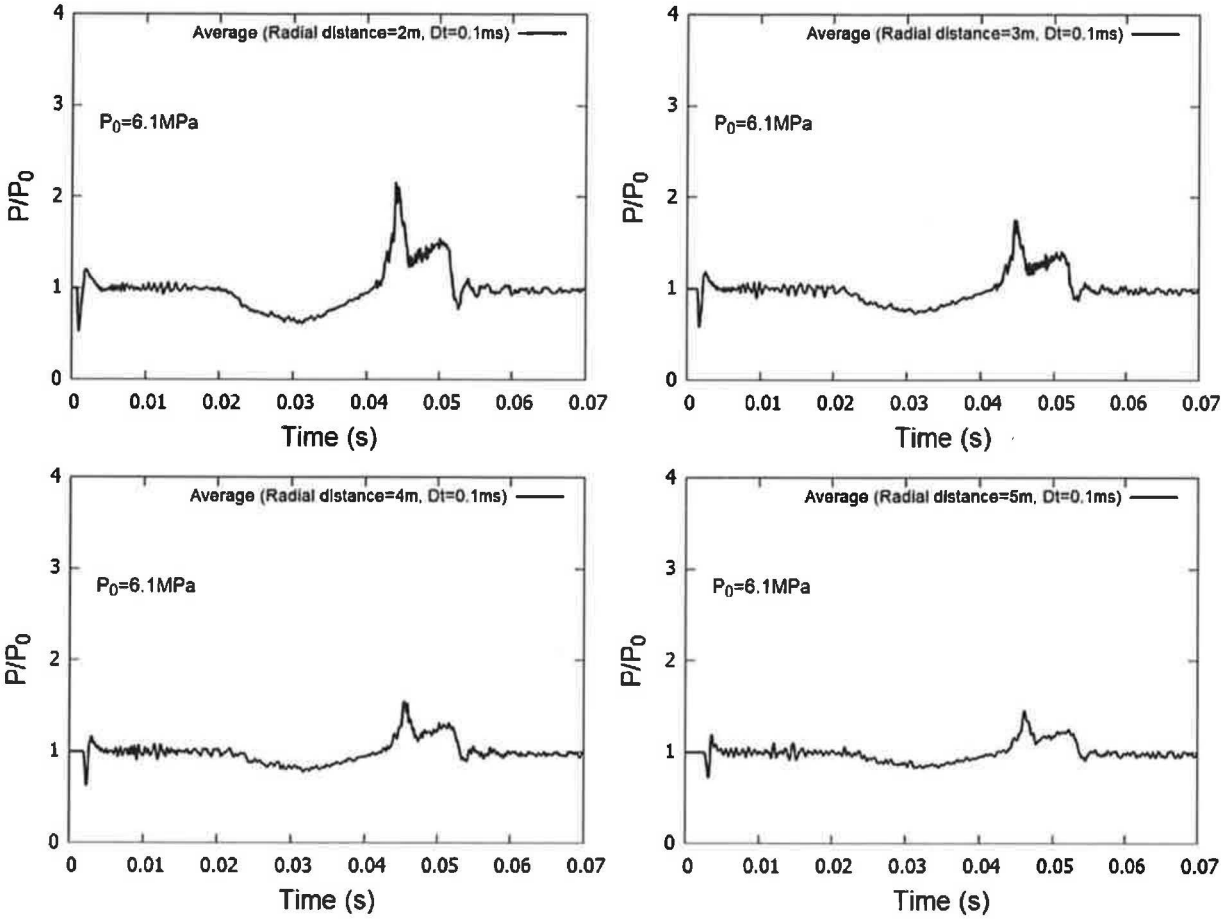

Fig. 23 Pressure time-histories at different radial distance of the steel cylinder with $Dt = 0.1$ ms

27, 28 clearly shows the effect of FSI in association with the collapsing speed on the buckled mode shape.

The normalized pressure time-history was compared in Fig. 29 for three different densities of the steel cylinder. The result showed that the original density gave the larger peak pressure than higher densities.

The average radial velocity of the mid-section of the steel cylinder was plotted in Fig. 30 for three different densities. The original density gave a velocity increase at much earlier time and the magnitude of the peak value was also higher.

The maximum areal shock energy density rate was also plotted for three different densities of the steel cylinder at the radial distance 2 m along different orientations along the circumference in Fig. 31. The maximum areal shock energy density rate was the largest for the original density case, and the smallest for the threefold density case. The fivefold density case gave the maximum areal shock energy density rate between the other two cases. Figures 27 and 31 have a common feature such that the largest maximum areal shock energy density rate was relatively uniform along the circumferential direction.

4.3 Implosion of aluminum cylinders

Aluminum cylinders were studied next. The geometry and the pressure loading were the same as those for both aluminum and steel cylinders, while their material properties were different. The first study was the change in the internal pressure of the aluminum cylinder as studied for the steel cylinder. The internal pressure was reduced in different rates, while the cylinder was subjected to water pressure on its outside. The buckled cross section is compared in Fig. 32 for four different rates of Dt. The results showed that the initially buckled shape was very dependent on the reduction rate of the internal pressure.

Figure 33 shows the normalized pressure time-history with $Dt = 5$ ms. Along the pressure plot, the buckled shape of the aluminum cylinder was also provided at some critical times. Until around 7 ms, the pressure was almost constant

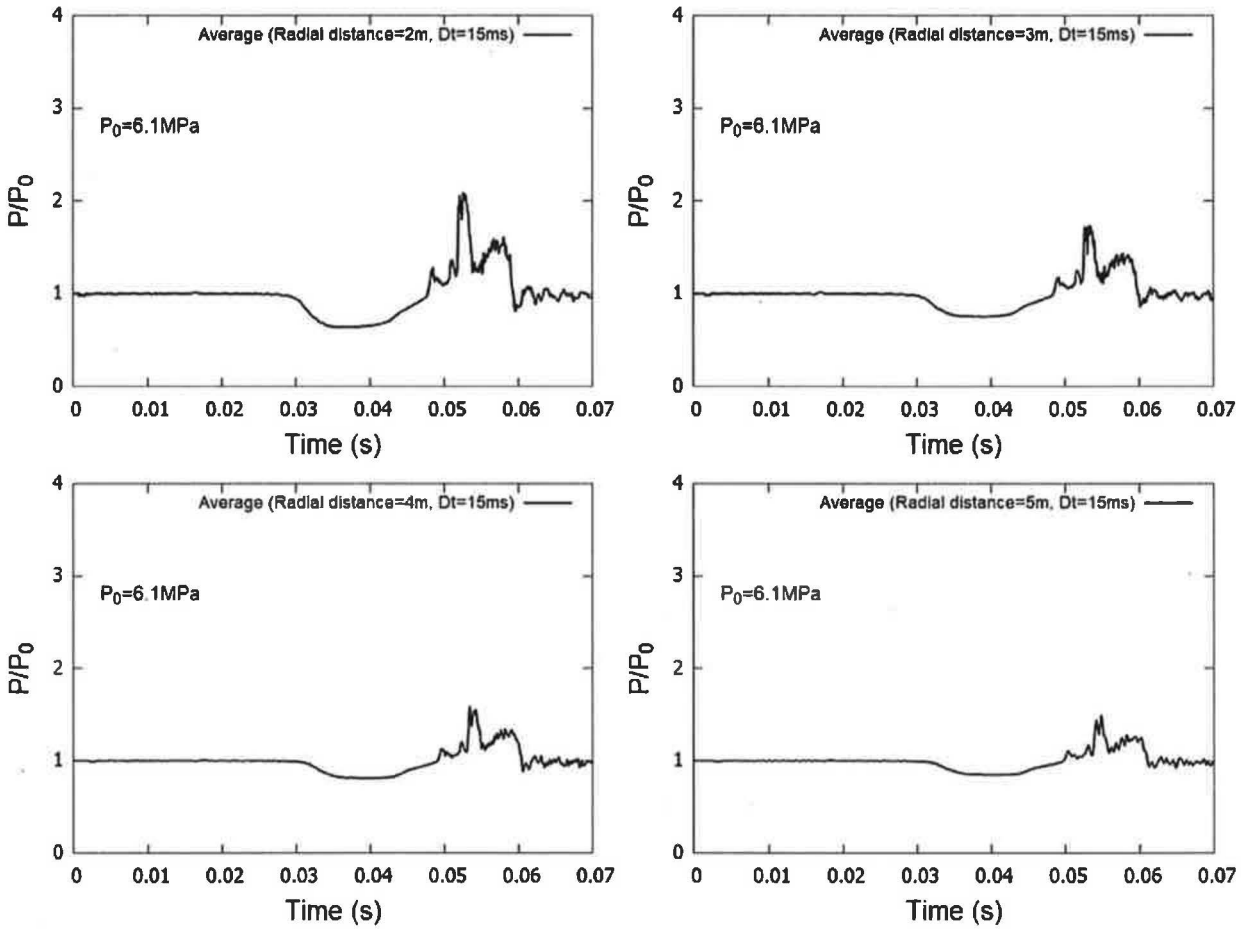

Fig. 24 Pressure time-histories at different radial distance of the steel cylinder with $Dt = 15$ ms

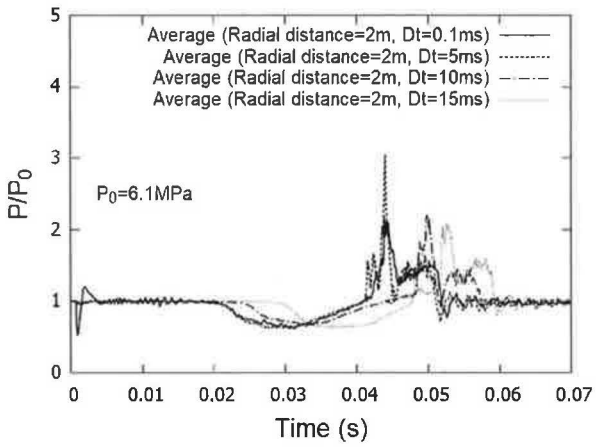

Fig. 25 Comparison of pressure time-hostories of steel cylinder for different reduction rates of internal pressure

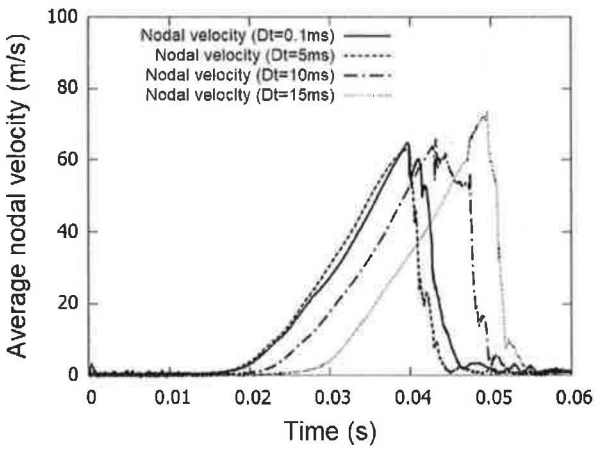

Fig. 26 Plot of averge radial velocity at the mid-section of steel cylinder with different reduction rates of the internal pressure

and started decrease quickly until 12 ms. Since then, pressure gradually increased until around 25 ms. The cross section at the mid-length clearly showed the buckled mode at 20 ms. The peak pressure was 2.9 times greater than the initial water

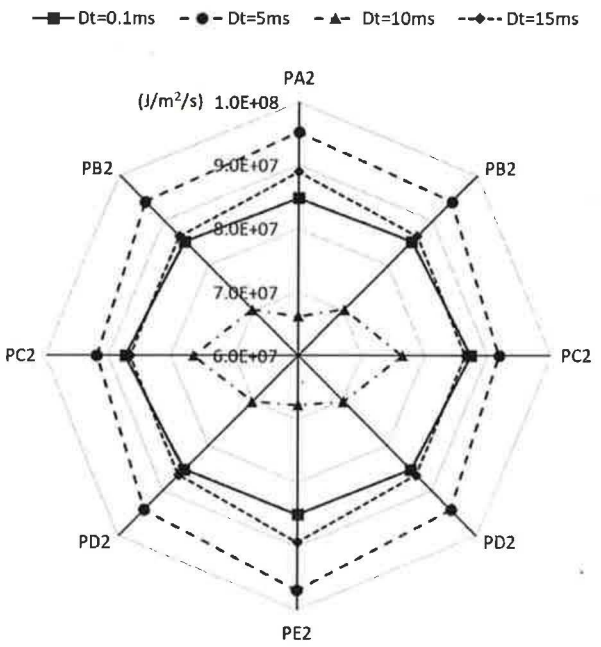

Fig. 27 Plot of areal wave energy density rate at diiferent gage locations along the circumferential direction for different reduction rates of the internal pressure of steel cylinder

pressure. After the first peak, the pressure dropped almost instantly, and then it reached the second peak at 33 ms. Then, the pressure dropped quickly and remained at the initial pressure level. The buckled cross section is also shown at each peak pressure. Even though the aluminum cylinder showed a major collapse at the first peak, it collapsed completely at the second peak except for the rigid end plate.

The pressure time-history for $Dt = 0.1$ ms shows a very high first peak followed by the secondary peak as shown in Fig. 34. The first peak pressure was about 2.5 times of the initial water pressure, which was even greater than that from the collapse of the steel cylinder. The second peak was about 2.5 times of the initial water pressure. Figure 35 shows all the pressure plots for different rates of internal pressure reduction. When comparing all the cases, the case with $Dt =$ 5 ms resulted in the largest peak pressure.

The average radial velocity at the mid-section of the aluminum cylinder was plotted in Fig. 36 for different Dt rates. The maximum peak velocity occurred for $Dt = 10$ ms and the minimum peak velocity was for $Dt = 15$ ms. The case with $Dt = 0.1$ ms and $Dt = 5$ ms gave almost the same of peak velocity. Comparing Figs. 35 and 36 suggested that there was no clear correlation between the maximum peak pressure and the maximum peak velocity.

When the pressure curves were compared between the aluminum and steel cylinders, the aluminum cylinder produced the peak pressure at earlier times, because it collapsed quicker due to lower stiffness and strength than the steel

Fig. 28 Buckled shapes of steel cylinders with three diferent assmed densities with FSI

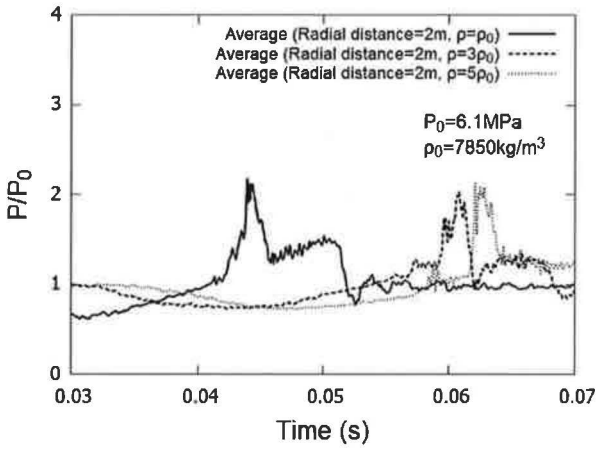

Fig. 29 Average pressure time-history for steel cylinder with different mass densities

cylinder. Another difference was the number of major peaks. The implosion of steel cylinder produced a single major pres-

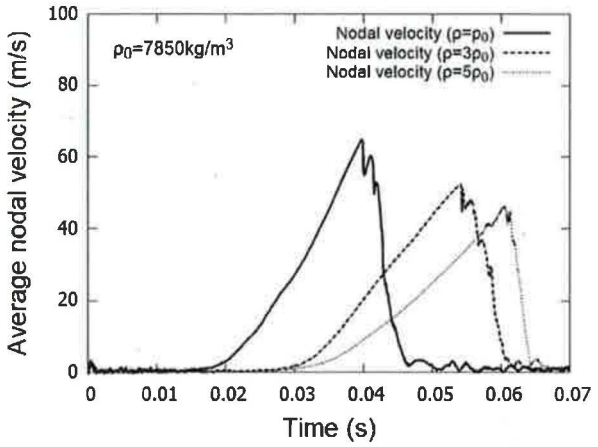

Fig. 30 Average nodal radial velocity at the mid-section of the steel cylinder with three different assumed densities

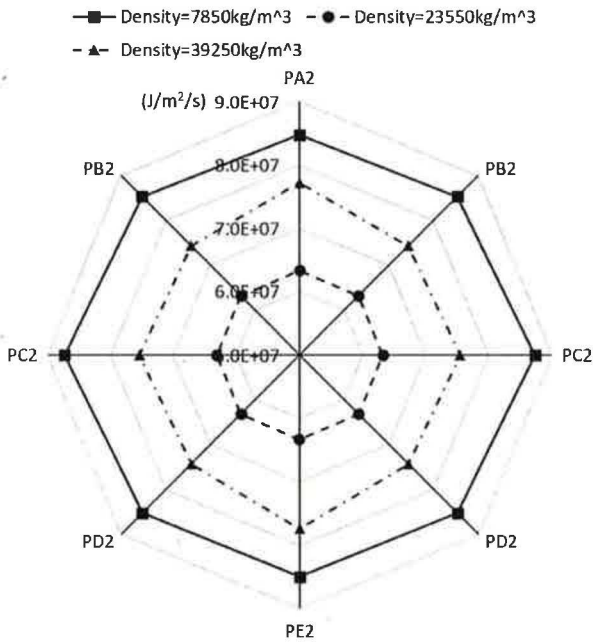

Fig. 31 Plot of areal wave energy density rate at diiferent gage locations along the circumferential direction for different mass densities of steel cylinder

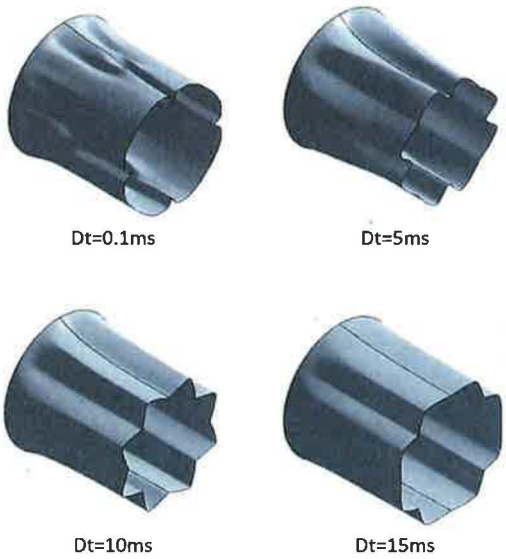

Fig. 32 Buckled mode shapes of aluminum cylinder under water as the inetrnal pressure decreased in different rates with FSI

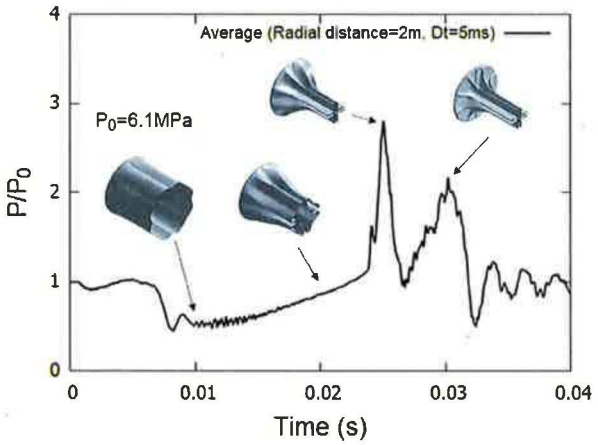

Fig. 33 Normalized pressure time-history of a cylindrical aluminum shell with inner radius 1 m, thickness 20 mm and $Dt = 5$msec

sure peak, while the aluminum cylinder resulted in two major peaks of comparable magnitude.

The density of the aluminum cylinder was arbitrarily changed to find its effect on the bucked shape and the resultant pressure wave. The cylinder was subjected to initial water pressure on its outer surface and air pressure on its inner surface without any additional internal pressure control. Figure 37 shows the cross section of the buckled aluminum cylinder with three different assumed mass densities. One was the original mass density, and the other two were threefold and fivefold densities. As the density was increased, the Fig. 37 shows that the buckled cross section varied. For example, the cross-sectional shape of the original density 2700 kg/m^3 was different from the buckled shapes with higher mass densities.

The average of normalized pressure time-history at the radial distance 2 m was plotted in Fig. 38 for the aluminum cylinder with the mass density varied. The magnitude of the peak pressure occurred with the highest density case among all three cases even though it occurred at a latest time.

Like the control of the internal pressure, the original density case showed two major peaks in the pressure time-history plot. The control of the internal pressure gave two major peaks one after the other, while the change in the density gave the second peak much later after the first peak. The

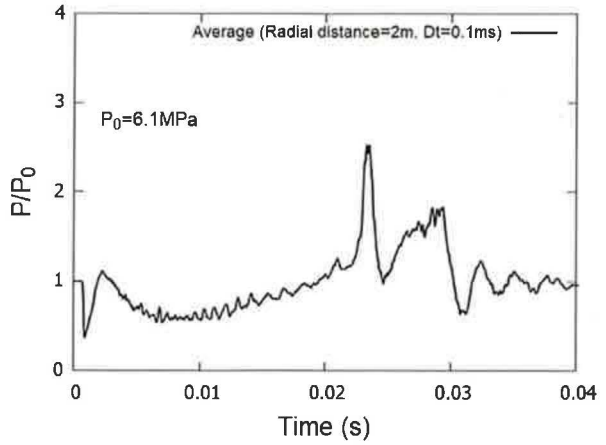

Fig. 34 Normalized pressure time-history of aluminum cylinder with $Dt = 0.1$msec

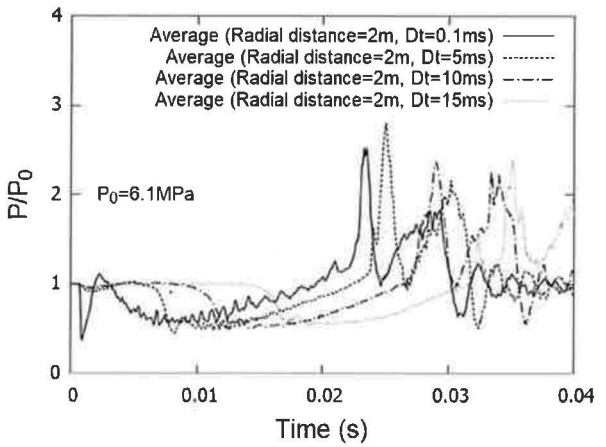

Fig. 35 Comparison of pressure time-histories of aluminum cylinder with different Dt rates

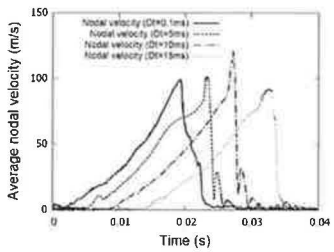

Fig. 36 Average nodal radial velocity at the mid-section of the aluminum cylinder with different Dt rates

second major peak was about two-thirds of the first major peak. However, the relative magnitude of the second peak to the first peak became smaller as the density increased. For the fivefold mass density case, the second major peak was much smaller than the first main peak. The results suggested that the second peak was related to the mass density of the

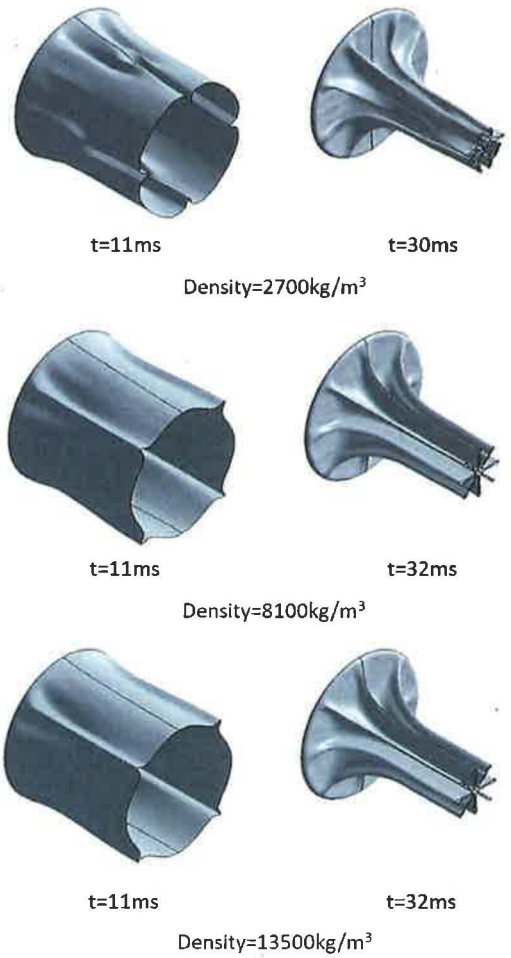

Fig. 37 Buckled shapes of aluminum cylinder with three assumed mass densities

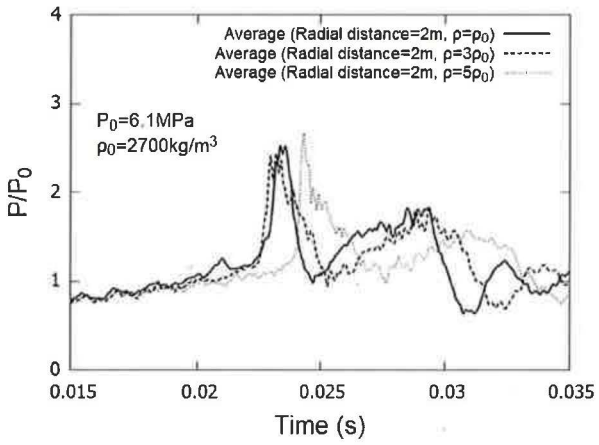

Fig. 38 Average pressure time-history at the radial distance 2 m for aluminum cylinder with different mass densities

material. If the mass density was greater than a certain value, the second peak became negligible. That also confirmed that

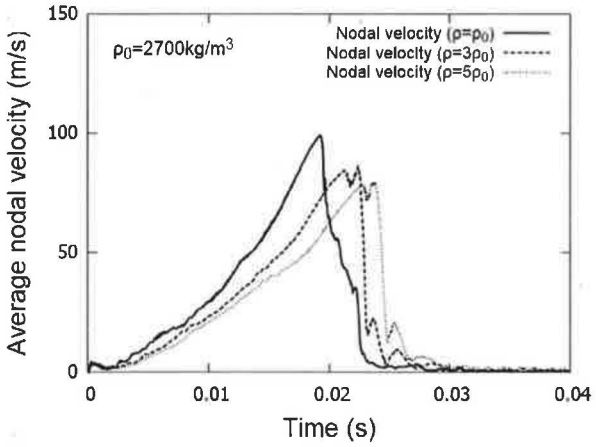

Fig. 39 Average nodal radial velocity at the mid-section of the aluminum cylinder with three different assumed densities

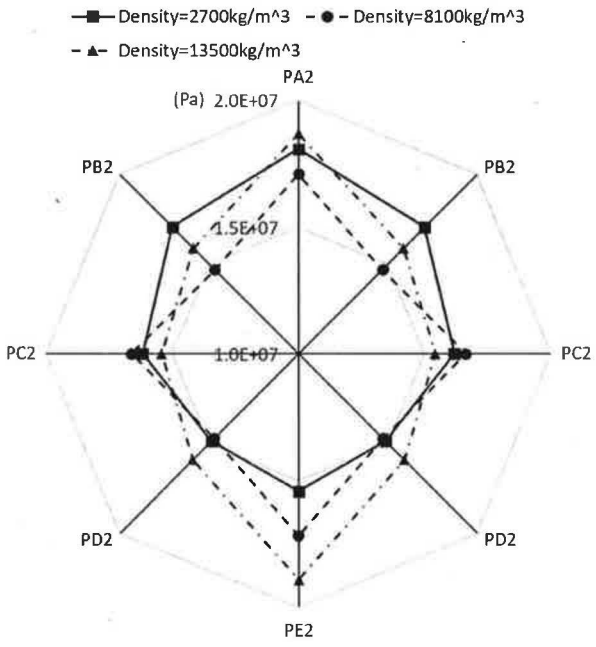

Fig. 40 Peak pressure of aluminum cylinder at 2 m with different mass densities

the steel cylinder showed a single major peak because of a higher mass density.

The average radial velocity at the mid-length of the aluminum cylinder is shown in Fig. 39 for three different assumed densities. The original density of the aluminum had the highest velocity with a rise at a shorter time period, while the fivefold density had the lowest velocity and a longer period. There was no clear correlation between the higher peak pressure and the radial velocity of the mid-section of the cylindrical shell.

The variation of the maximum pressure at the radial distance of 2 m was plotted for three different densities of the

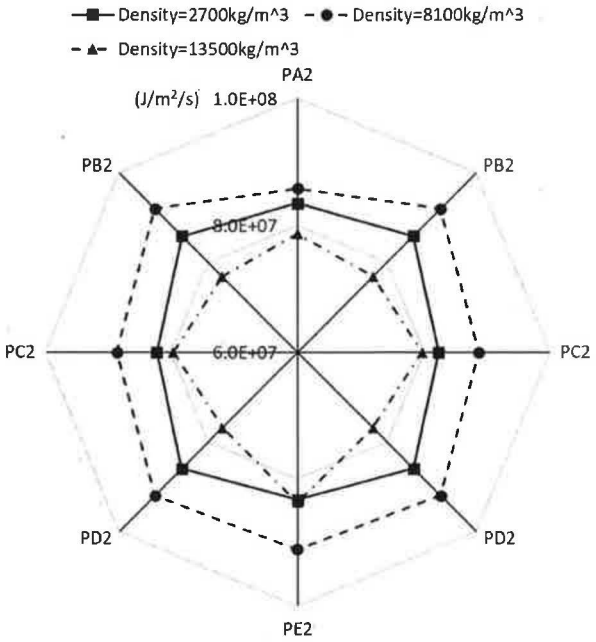

Fig. 41 Maximum areal shock energy density rate of aluminum cylinder at 2 m with different mass densities

aluminum cylinder in Fig. 40. The case of the original density showed a quite uniform pressure distribution around the circumference of the cylinder. On the other hand, the other two cases gave higher pressure at the gage locations #PA2 through #PE2. These results are believed to be linked to the buckled shaped as shown in Fig. 37. The last two cases showed the same buckled shape, while the original density case yielded a different shape of buckling.

The maximum areal shock energy density rate was quite uniform around the circumference of the cylinder regardless of the assumed density of the aluminum cylinder, as shown in Fig. 41. The maximum areal shock energy density rate was greater for the threefold density and the least for the fivefold density. This could result from the fluid velocity. Figure 42 shows the fluid radial velocity time-history. The plot shows the highest velocity for the original density and the lowest velocity for the fivefold density.

4.4 Implosion of composite cylinders

The carbon composite cylinder was subjected to the same external water pressure as the previous metallic cylinders. As before, the study of the internal pressure reduction was conducted first. Figure 43 compares the buckled cross section of the composite cylinder as the internal pressure was reduced in different rates. The buckling mode was $n = 12$ for $Dt = 0.1$ ms, a very quick decrease in the internal pressure. Other cases had the bucking mode $n = 8$ as the Dt increased.

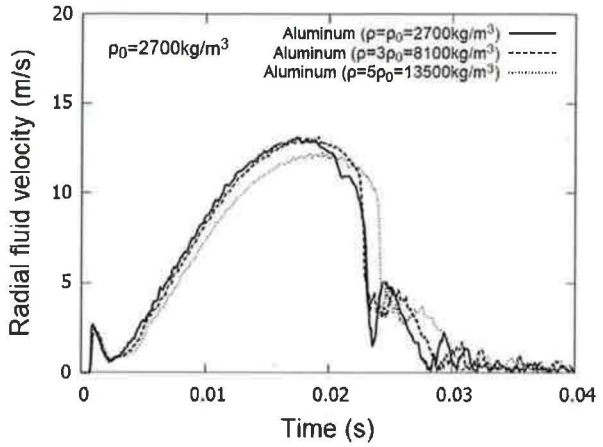

Fig. 42 Radial fluid velocity time-history of aluminum cylinder of different mass densities at 2 m of radial distance

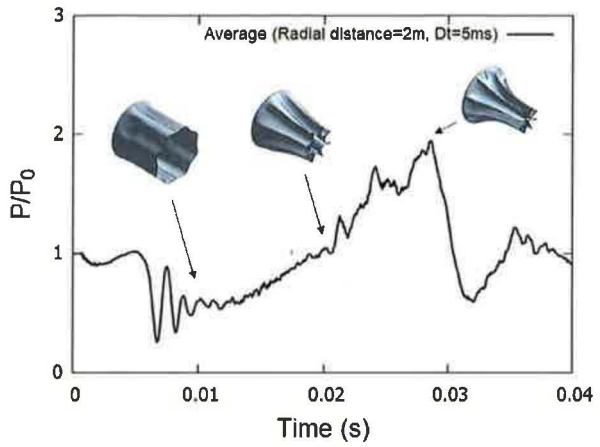

Fig. 44 Normalized pressure time-history of a composite cylinder with inner radius 1 m, thickness 20 mm and Dt = 5msec

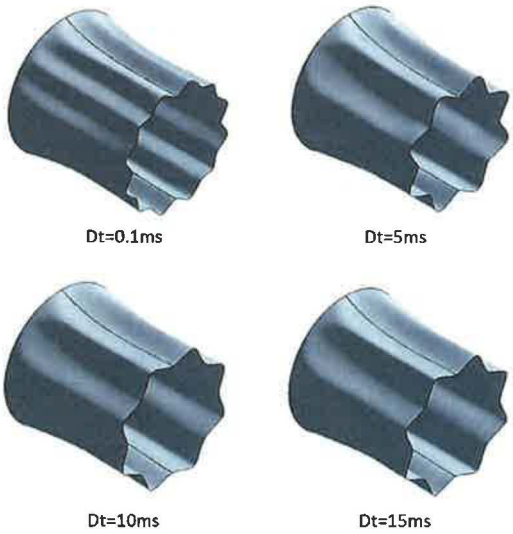

Fig. 43 Buckled mode shapes of composite cylinder under water as the inetrnal pressure decreased in different rates with FSI

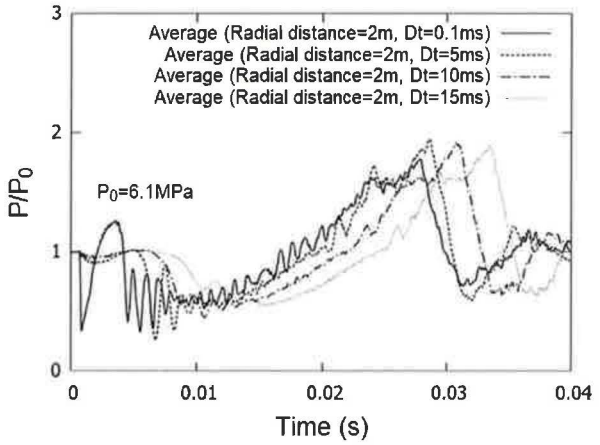

Fig. 45 Comparison of pressure time-histories of composite cylinder with different Dt rates

The pressure time-history resulting from the implosion of the composite cylinder was plotted in Fig. 44 when Dt = 5.0 ms. The collapsing cross-sectional views were also provided in the plot. The pressure curve for the composite cylinder was quite different from those for the metallic cylinders. The pressure showed a large oscillation during the very early buckling stage, and the pressure increased gradually to the peak pressure. There was neither a long duration of almost constant pressure nor a sudden increase of the pressure to the peak values. The maximum peak pressure occurred earlier than the steel cylinder but later than the aluminum cylinder.

Figure 45 shows the all pressure plots for different reduction rates of the internal pressure. The case with $Dt = 0.1$ ms had the smallest peak pressure, while the case with Dt = 5.0 ms resulted in the largest peak pressure. The other two cases were very close to the latter case. In addition, the case with $Dt = 0.1$ ms gave a very oscillatory pressure from the beginning to a quite later time.

The average nodal radial velocity at the mid-section of the composite cylinder was compared in Fig. 46 for different Dt rates. In this case, the magnitude of the peak radial velocity agreed with the magnitude of the peak pressure qualitatively. In other words, Dt = 5.0 ms gave the largest peak pressure as well as the largest peak radial velocity, while $Dt = 0.1$ ms gave the smallest peak pressure as well as the smallest peak radial velocity. The other two cases were also similar. The composite cylinder was the only case showing such a correlation between the peak pressure and peak radial velocity. The metallic cylinders did not show such a correlation.

As the second parametric study, the mass density of the carbon composite cylinder was also varied to three and five times of the original density. Figure 47 compares the buckled cross sections with different mass densities. The buckled

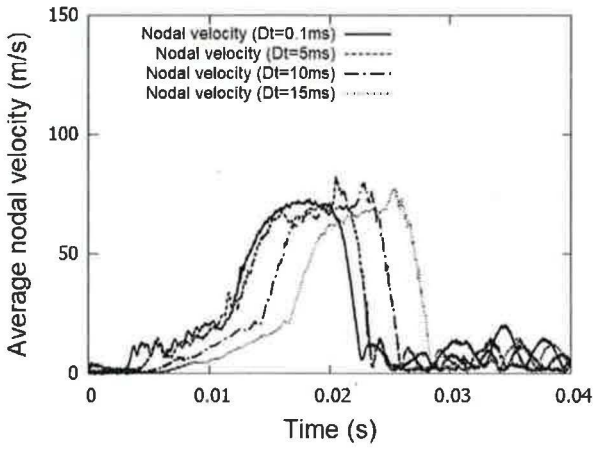

Fig. 46 Average nodal radial velocity at the mid-section of the composite cylinder with different *Dt* rates

cross sections were same though the original density to fivefold density and the wave number was 12.

The pressure time-history of the composite cylinder with the original mass density is shown in Fig. 48. The pressure was the average of five gages located at 2 m away from the center of the cylinder. The pressure profile of the composite cylinder was quite different from those of the aluminum and steel cylinders. Both metallic cylinders resulted relatively constant pressure with small variations until very close to the peak pressures except for the initial sudden dip at very early times. Such a long period of small changes in the pressure with sudden peaks occurred for all the parametric studies regardless of the change in the reduction rate of the applied internal pressure or a change in the mass density of both metallic cylinders. On the other hand, the composite cylinder showed a continuous variation of pressure until the peak pressure. The peak pressure was reached more gradually rather than suddenly. This suggests that the buckling and collapse of the composite cylinder was more gradual than the metallic cylinders until the complete collapse. The failure progress in polymer composites was generally very gradual rather than very sudden. Such a failure behavior resulted in very different implosion pressure behavior as shown in Fig. 48.

The peak pressure was about 1.8 of the initial water pressure, which was lower than those of the metallic cylinders. The gradual increase reduced the peak pressure. However, the integration of pressure over time, i.e., pressure impulse, was much greater for the composite cylinder because of a longer duration of gradual increase of the pressure. As the density was increased for the composite cylinder, the peak pressure decreased. When the mass density was assumed fivefold, the peak pressure was about 1.7 times of the initial pressure. However, the general pressure time-history was similar regardless of the mass density except that the higher density resulted in a longer duration of the pressure increase to the

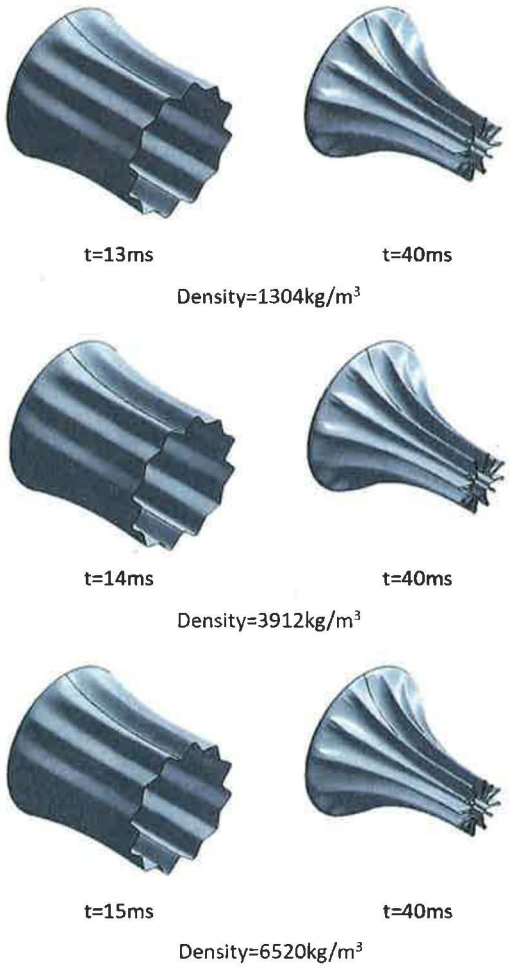

Fig. 47 Buckled cross section at the mid-section of composite cylinder with different assumed mass densities

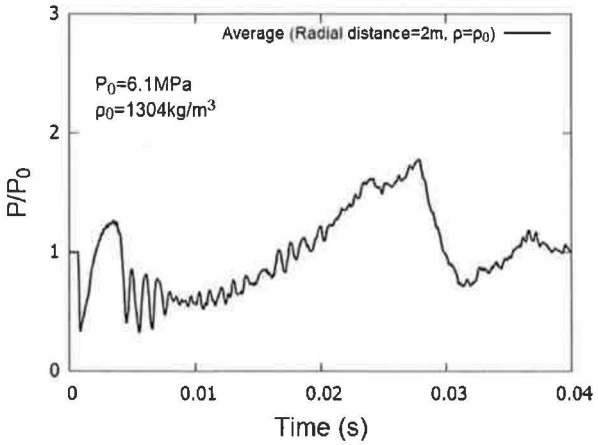

Fig. 48 Normalize pressure time-history of composite cylinder with the original mass density

peak value as seen in Fig. 49. Therefore, even though the peak pressure was lower for the higher mass case, the pres-

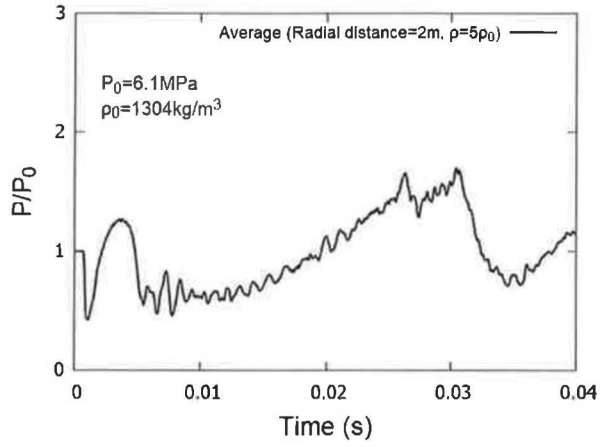

Fig. 49 Normalize pressure time-history of composite cylinder with fivefold mass density

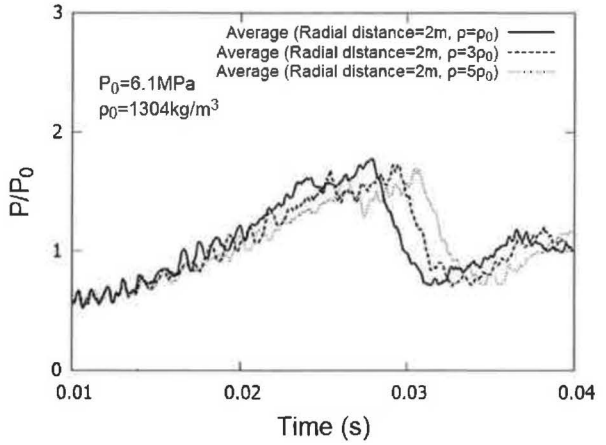

Fig. 50 Average pressure time-history at the radial distance 2 m for composite cylinder with different mass densities

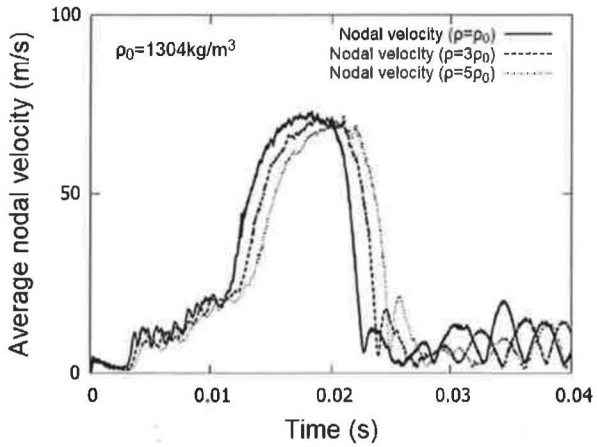

Fig. 51 Comparison of nodal velocity time history with different density of composite cylinder

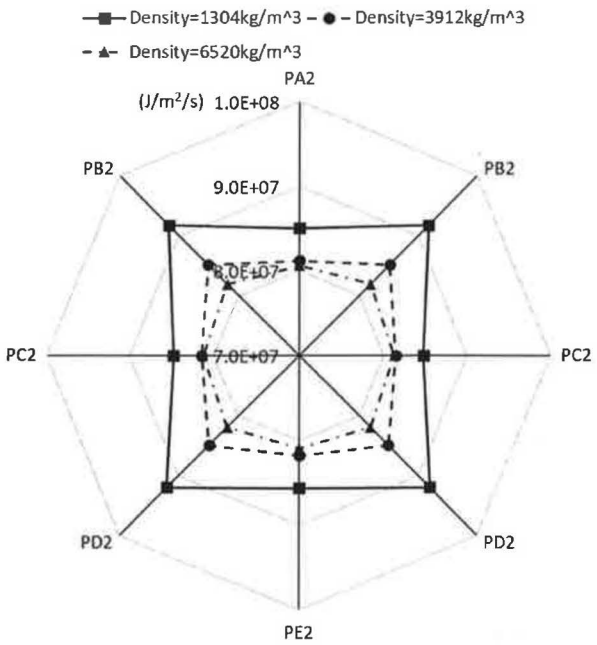

Fig. 52 Maximum shock energy areal density rate of composite cylinder at 2 m with different mass densities

sure impulse was relatively the same as that of the original mass.

The average of normalized pressure time-history at the radial distance 2 m was plotted in Fig. 50 for the composite cylinder with the mass density varied.

Figure 51 compares the average radial velocities of the composite cylinders at the mid-section for three different mass densities. The original density case had the highest peak velocity than the other cases. The threefold and fivefold density cases were very similar except that the velocity curve was slightly delayed in time for the fivefold case than the threefold case.

The maximum shock energy areal density rate was plotted in Fig. 52. The maximum shock energy areal density rate was the largest for the original mass case and decreased as the mass density increased.

4.5 Implosion of cylinders with initial defect

Because cylinders made of different materials showed different buckling modes, they could not be compared on the same baseline. As a result, an initial defect was applied to all cylinders so that their buckling mode shapes could be identical. To that end, an imperfection of the wall thickness was introduced along the longitudinal direction of the cylinders as sketched in Fig. 53. The defect was introduced as a thinner wall thickness because this was easier to model rather than the change in the cross-sectional geometry. The defect

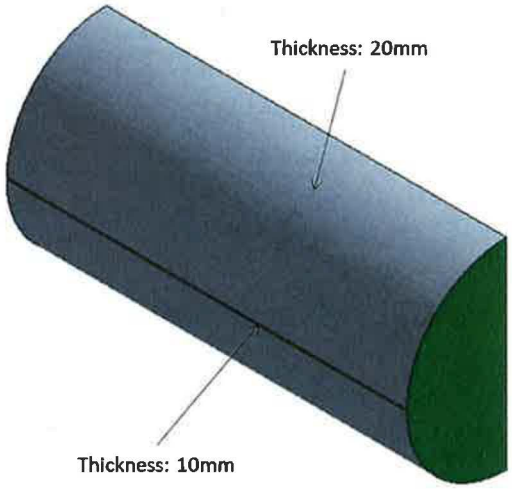

Fig. 53 A half cylinder model with initial defect along the longitudinal direction

was located at the midway of the circumference such that the major buckled mode would be $n = 2$.

First, the dynamic buckling analysis of the cylinders was conducted to check the buckling mode. Figure 54 compares the buckled mode shapes of three different cylinders made of steel, aluminum, and composite materials, respectively, under the same pressure loading condition, but not with FSI. The buckled cross-sectional shapes were very close one another.

Similarly, Fig. 55 shows the buckled and collapsed cylinders with FSI for the implosion process. The figure shows both early time and late time of the buckling. Even though the initial defect was introduced, the buckled cross-sectional shapes were different, especially for the composite cylinders.

The resultant pressure during the implosion process of the three cylinders with the same defect was plotted in Fig. 56. In this case, the aluminum cylinder yielded the greatest peak pressure followed by the composite cylinder. The steel cylinder produced the least peak pressure. The composite cylinder showed a more gradual pressure build-up until the first peak pressure which occurred earlier than other cylinders. The aluminum cylinder showed two major peaks one after the other. However, in this case, the second peak was the maximum pressure, while the previous case showed the maximum pressure at the first peak as seen in Fig. 34. Such a difference must be caused by the buckled/collapsed shapes of the cross

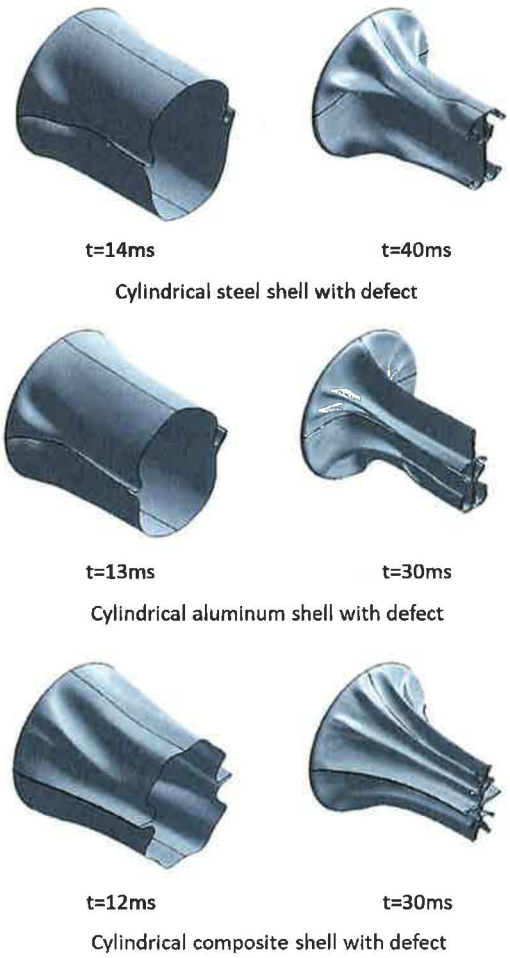

Fig. 55 Dynamically buckled mode shapes for three different cylinders with initial defect with FSI

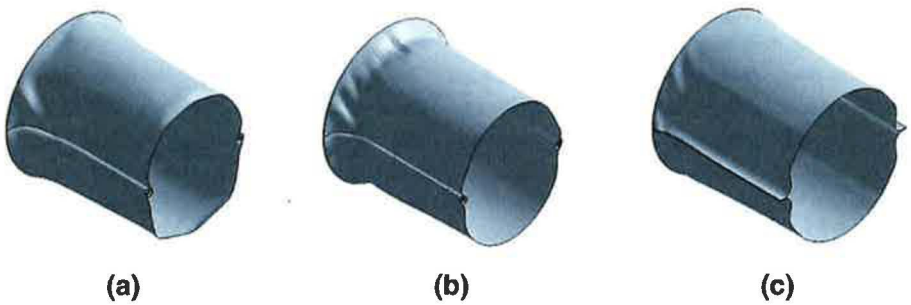

Fig. 54 Dynamically buckled mode shapes for **a** steel, **b** aluminum and **c** composite cylinders without FSI

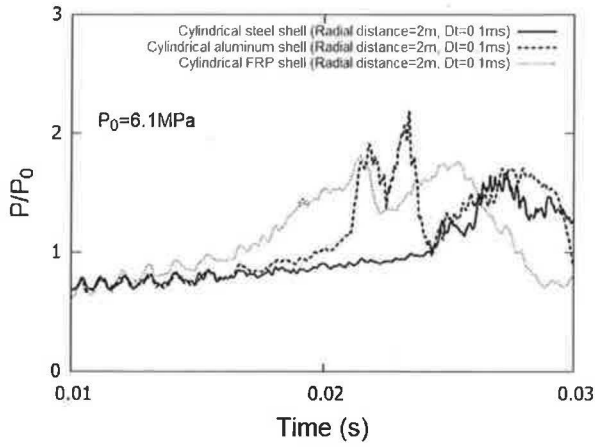

Fig. 56 Normalized pressure from collapse of three different cylinders with the initial defect under the same initial pressure with $Dt = 0.1$msec

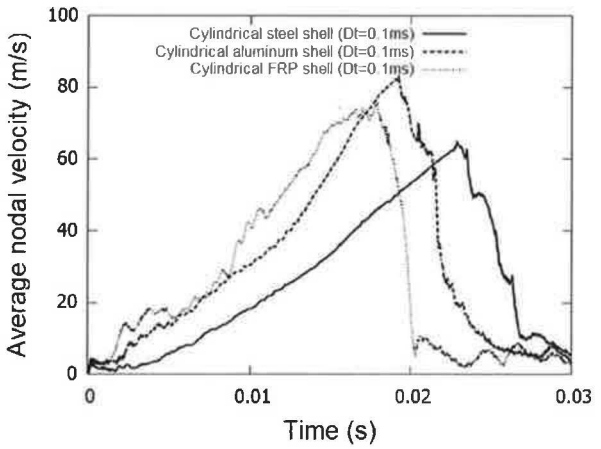

Fig. 57 Comparison of the average nodal velocity of the mid-section of three different cylinders with the initial defect under the same initial pressure with $Dt = 0.1$msec

sections, because the introduction of a defect changed those shapes.

Finally, Fig. 57 compares the average nodal velocity of the mid-section of each cylinder during the implosion process. The peak velocity and its timing agreed with the peak pressures in Fig. 56 at least qualitatively. This result suggested that when the buckled/collapsed shapes were close, the collapsing speed influenced the peak pressure and timing resulting from the implosion. However, when the collapsing shapes were different, there was no such a direct correlation between the collapsing speed of the cross section and the resultant peak pressure.

5 Conclusions

A series of numerical studies were conducted for implosion of spherical and cylindrical shells. First, static buckling of the shell structures was conducted followed by their dynamic buckling. Then, the implosion was studied using the FSI between the shell structures and both internal and external fluids. The external fluid was water at a given depth, while the internal fluid was air at the atmospheric pressure initially.

The finally collapsed shape of the spherical shell was very complex because the whole surface of the spherical shell should be shrunken into a much smaller space. There were many wrinkles and self-contacts of the collapsed surface. Therefore, the analysis program stopped because of such a complex bucked shape. To overcome this problem, the element erosion option should be considered. Then, some deleted elements resulting from too much straining helped the program continue beyond the complete collapse of the spherical shell. On the other hand, the element erosion option was not necessary for the cylindrical shells.

Under the same external pressure, the implosion of the aluminum spherical shell induced about 1.1 times higher peak pressure than the steel shell of the same geometry. The peak pressure also occurred at around 40 ms for the steel shell and around 30 ms for the aluminum shell.

Buckling mode shapes of cylindrical shells were varied depending on the reduction rate of the internal pressure. This statement was true whether there was FSI or not. When cylinders were bucked quickly, the mode shape was $n = 6$, and the buckling was much slowed, the buckling mode changed to $n = 4$, which was the static buckling mode of the steel cylinder.

The buckled mode shapes without FSI were not the same as those with FSI. Without FSI, a change in the mass density did not affect the buckling mode of the steel and aluminum cylinder. Composite cylinder showed some small effects on the complex buckled shapes. With FSI, a change in the mass density of the steel changed the buckled mode shapes. Aluminum shell also showed some changes in the buckled shapes. In addition, the buckled mode shapes were very different depending on the materials such as steel, aluminum, or laminated composite.

All the numerical simulations showed that there was an optimal buckling condition during the implosion, which resulted in the largest peak of the resultant shock wave. In other words, the fastest dynamic buckling did not necessarily result in the largest peak pressure. The aluminum cylinder showed that the largest peak pressure occurred with the fastest buckling of the cylinder.

With FSI, the steel cylinder showed one major peak in the pressure time-history during implosion, while the aluminum cylinder showed two major peaks. In some case, the two peaks had comparable magnitudes. The aluminum cylinder

collapsed completely at the second major peak. As the density of the aluminum increased as a parametric study, the second peak became smaller. This suggested that the second peak is related to the mass densities of the cylinder.

The shock pressure time-history due to the implosion of the composite cylinder was significantly different from those of metal cylinders. The pressure graph of the composite cylinder showed more gradual and oscillatory behavior with much lower peak pressure as compared to the metallic cylinders of the same size.

To compare three cylinders made of different materials with the same baseline, an initial defect was introduced to all cylinders to generate the same or close shapes of buckling modes. The study showed that the aluminum cylinder gave the largest peak pressure, while the steel cylinder gave the least peak pressure. The peak pressure of the composite cylinder was between the two cases. The study showed that the peak pressure during implosion was related to the collapsing velocity if the buckling shapes were similar. However, different modes of buckling did not suggest such a direct correlation between the peak pressure and collapsing speed of the cylindrical shells. Then, the combination of the buckled mode shapes and collapsing speed affected the resultant shock pressure.

Acknowledgements One of the coauthors, Y.W. Kwon, acknowledged the financial support from the Solid Mechanical Program of Office of Naval Research. The Program Manger is Dr. Yapa Rajapakse.

Compliance with ethical standards

Conflict of interest On behalf of all authors, the corresponding author states that there is no conflict of interest.

References

Farhat C, Wang KG, Main A, Kyriakides S, Lee L-H, Ravi-Chandar K, Belytshko T (2013) Dynamic implosion of underwater cylindrical shell: experiments and computations. Int J solids Struct 50:2943–2961

Gilmore FR (1952) The growth of collapse of a spherical bubble in a viscous compressible liquid, Hydrodynamic laboratory, California Institute of Technology, California

Gupta S, Parameswaran V, Sutton MA, Shukla A (2014) Study of dynamic underwater implosion mechanics using digital image correlation. Proc R Soc Math Phys Eng Sci 470(2172):20140576

Ilinskii YA, Zabolotskaya EA, Hay TA, Hamilton MF (2012) Models of cylindrical bubble pulsation. J Acoust Soc Am 132:1346

Isaacs JD, Maxwell AE (1952) The ball-breaker, a deep water signaling device. J Mar Res 11:63–68

Kedrinskii VK (2005) Hydrodynamics of explosion: Experiments and Models. Springer, Berlin, Heidelberg, New York

Krueger SR (2006) Simulation of cylinder implosion initiated by an underwater explosion, Naval Postgraduate School, Monterey

Livemore Software Technology (LST) (2019), LS-DYNA Theory Manual. LST web site. https://www.lstc.com/download/manuals

Orr M, Schoenberg M (1976) Acoustic signatures from deep water implosions of spherical cavities. J Acoust Soc Am 59(5):1155–1159

Pinto M, Gupta S, Shukla A (2015) Hydrostatic implosion of GFRP composite tubes studied by digital image correlation. J Press Vessel Technol Oct 137(5):051302

Pinto M, DeNardo NA, Shukla A (2018) Geometric impact on the implosion energy and failure mechanics of carbon composite tubes, Multiscale and Multidiscip. Model Exp and Des 1:171–179

Plesset MS (1949) The dynamics of cavitation bubbles. J Appl Mech 16:228–231

Rayleigh L (1917) On the pressure developed in a liquid during the collapse of a spherical cavity. Philoso Mag 34:94–98

Sugimoto S, Kwon YW (2020) Implosion of spherical and cylindrical air cavities. Multiscale Multidiscip. Model. Exp. and Des. https://doi.org/10.1007/s41939-020-00074-2

Timoshenko SP, Gere JM (1961) Theory of elastic stability. McGraw-Hill, New York

Turner SE (2007) Underwater implosion of glass spheres. J Acoust Soc Am 121(2):844–852

Turner SE, Ambrico JM (2012) Underwater implosion of cylindrical metal tubes. J Appl Mech 80(1):011013

Urick RJ (1963) Implosions as sources of underwater sound. J Acoust Soc Am 35(12):2026–2027

Windenburg DF, Trilling C (1934) Collapse by instability of thin cylindrical shells under external pressure. Trans ASM, APM 56–20:819–825